Cell

Article

A blood-brain barrier-like vascular gate limits immunotherapy efficacy in neuroendocrine cancers

Graphical abstract

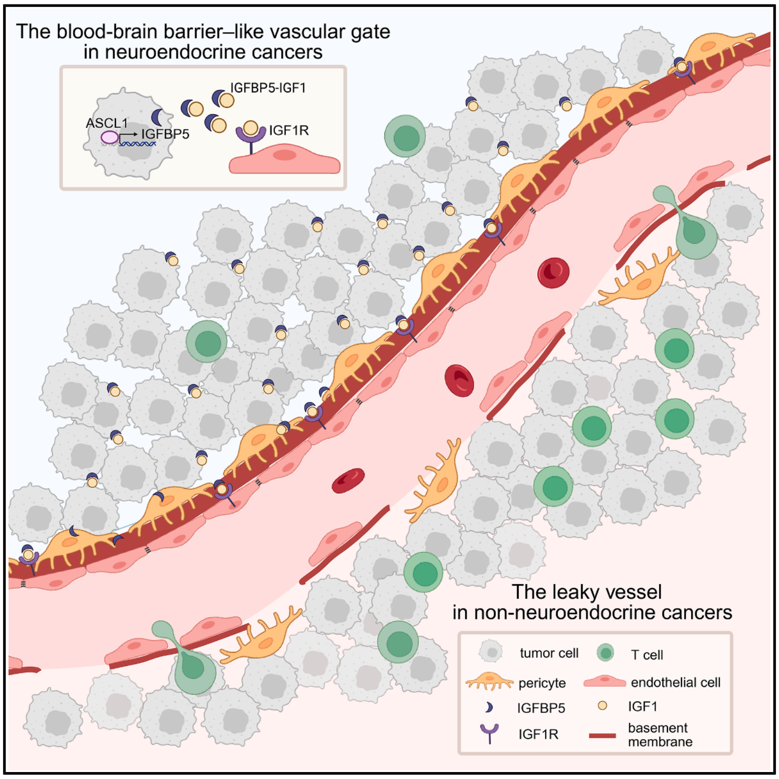

Authors

Yiyun Wang (王怡匀), Ailing Zhong (钟艾伶), Bo Wang (王博), ..., Manli Wang (王漫丽), Yu Liu (刘玉), Chong Chen (陈崇)

Correspondence

zhang.yan@scu.edu.cn (Y.Z.),
nafeifei@foxmail.com (F.N.),
manli_wang123@sina.com (M.W.),
yuliuscu@scu.edu.cn (Y.L.),
chongchen@scu.edu.cn (C.C.)

In brief

A blood-brain barrier-like vascular gate in small cell lung cancer and other neuroendocrine cancers blocks immune cells and drives resistance to immunotherapy. Targeting the proteins IGF1R or IGFBP5 boosts CD8$^+$ T cell infiltration and enhances anti-PD1 therapy.

Highlights

- Discovery of the BBB-like vascular gate (BVG) in SCLC
- The BVG is induced by SCLC tumor cells through the ASCL1-IGFBP5-IGF1R axis
- Targeting the BVG with OSI-906 synergizes with immunotherapy
- The BVGs are conserved across multiple NECs

Wang et al., 2026, Cell *189*, 1–18

https://doi.org/10.1016/j.cell.2026.04.017

Please cite this article in press as: Wang et al., A blood-brain barrier-like vascular gate limits immunotherapy efficacy in neuroendocrine cancers, Cell (2026), https://doi.org/10.1016/j.cell.2026.04.017

Cell

CellPress

Article

A blood-brain barrier-like vascular gate limits immunotherapy efficacy in neuroendocrine cancers

Yiyun Wang (王怡匀),[1,13] Ailing Zhong (钟艾伶),[1,13] Bo Wang (王博),[1,2,13] Xiaoqian Zhai (翟小倩),[3,4] Chang Lei (雷畅),[1] Zuoyu Liang (梁作禹),[5] Xintong Deng (邓馨童),[1] Jian Zhong (钟建),[6] Chaoxin Xiao (肖朝新),[1] Jianan Zheng (郑佳楠),[1] Baohong Wu (吴宝红),[1] Lanxin Zhang (张岚馨),[1] Yuying Wang (王昱颖),[1] Xiangmeng Luo (罗香梦),[1] Jian Wang (王健),[1] Mengsha Zhang (张梦莎),[1] Hongyu Liu (刘虹余),[1] Xudong Wan (万旭东),[1] Siqi Dai (代思琪),[1] Yucen Yang (杨玉涔),[1] Shiyu Zhang (张诗语),[7] Weiya Wang (王威亚),[5] Shengyong Yang (杨胜勇),[8] Jianxin Xue (薛建新),[1] Chengjian Zhao (赵成建),[8] Tuomas Tammela,[9] Zhiming Li (李治明),[10] Yan Zhang (张衍),[4,*] Feifei Na (纳飞飞),[1,*] Manli Wang (王漫丽),[2,*] Yu Liu (刘玉),[11,12,*] and Chong Chen (陈崇)[1,12,14,*]

[1]Department of Thoracic Oncology, State Key Laboratory of Biotherapy, Cancer Center, West China Hospital, Sichuan University, Chengdu, Sichuan 610041, China

[2]TCM Prevention and Treatment of Metabolic and Chronic Diseases Key Laboratory of Sichuan Province, Hospital of Chengdu University of Traditional Chinese Medicine, Chengdu, Sichuan 610072, China

[3]Department of Medical Oncology, Cancer Centre, West China Hospital, Sichuan University, Chengdu, Sichuan 610041, China

[4]Lung Cancer Center, Lung Cancer Institute, West China Hospital, Sichuan University, Chengdu, Sichuan 610041, China

[5]Department of Pathology, West China Hospital, Sichuan University, Chengdu, Sichuan 610041, China

[6]Peking University Chengdu Academy for Advanced Interdisciplinary Biotechnologies, Chengdu, Sichuan 610041, China

[7]Department of Urology, West China Hospital, Sichuan University, Chengdu, Sichuan 610041, China

[8]Department of Biotherapy, Cancer Center, State Key Laboratory of Biotherapy, West China Hospital, Sichuan University, Chengdu, Sichuan 610041, China

[9]Cancer Biology and Genetics Program, Sloan Kettering Institute, Memorial Sloan Kettering Cancer Center, New York, NY, USA

[10]West China School of Public Health, West China Fourth Hospital, State Key Laboratory of Biotherapy, Sichuan University, Chengdu, Sichuan 610041, China

[11]Department of Hematology, Institute of Hematology, State Key Laboratory of Biotherapy, West China Hospital, Sichuan University, Chengdu, Sichuan 610041, China

[12]Frontiers Medical Center, Tianfu Jincheng Laboratory, Chengdu, Sichuan 610212, China

[13]These authors contributed equally

[14]Lead contact

*Correspondence: zhang.yan@scu.edu.cn (Y.Z.), nafeifei@foxmail.com (F.N.), manli_wang123@sina.com (M.W.), yuliuscu@scu.edu.cn (Y.L.), chongchen@scu.edu.cn (C.C.)

https://doi.org/10.1016/j.cell.2026.04.017

SUMMARY

Small cell lung cancer (SCLC), a highly aggressive neuroendocrine malignancy, exhibits poor response to immunotherapy, and the underlying mechanisms remain unclear. Here, we identify a blood-brain barrier-like vascular gate (BVG) in SCLC, distinct from non-SCLC (NSCLC) and other cancers, composed of tightly connected endothelial cells, a thickened basement membrane, and dense pericyte coverage. Functionally, this blood-brain barrier-like vascular gate restricts immune cell infiltration, contributing to SCLC's immunotherapy resistance. Mechanistically, achaete-scute family basic-helix-loop-helix (bHLH) transcription factor 1 (ASCL1), the master transcription factor of SCLC, is essential for BVG formation by regulating insulin-like growth factor-binding protein 5 (IGFBP5), which activates the IGF1 signaling in endothelial cells. IGFBP5 knockout or treatment with the IGF1R inhibitor OSI-906 enhances CD8$^+$ T cell infiltration and synergizes with anti-PD1 therapy. Furthermore, this ASCL1-IGFBP5-IGF1R axis and the BVG are conserved across multiple neuroendocrine cancers (NECs). Our findings reveal a previously unrecognized vascular gate in NECs and propose novel therapeutic strategies to enhance immunotherapy efficacy in these recalcitrant cancers.

INTRODUCTION

Neuroendocrine cancers (NECs) are rare but highly aggressive malignancies.[1,2] NECs are highly heterogeneous, whereas the majority express achaete-scute family basic-helix-loop-helix (bHLH) transcription factor 1 (ASCL1), a critical transcription factor for neuroendocrine differentiation and a diagnostic marker for classical NEC subtypes.[3–7] These tumors are frequently associated with a predominantly immunosuppressive tumor microenvironment (TME), characterized by minimal infiltration of cytotoxic

Please cite this article in press as: Wang et al., A blood-brain barrier-like vascular gate limits immunotherapy efficacy in neuroendocrine cancers, Cell (2026), https://doi.org/10.1016/j.cell.2026.04.017

T cells.[8–10] Although some immunotherapies, such as durvalumab and atezolizumab, have been approved for the treatment of NECs—particularly small cell lung cancer (SCLC), one of the most common NEC subtypes—the clinical benefits remain limited. The IMpower133 and CASPIAN studies showed that atezolizumab and durvalumab, later approved by the Food and Drug Administration, moderately increased the survival of SCLC patients by about 2 months.[11,12] Of note, retrospective analyses suggested that the classical ASCL1$^+$ and/or NEUROD1$^+$ SCLC displayed even worse responses.[8] However, the mechanisms underlying the immunosuppressive features of NECs remain unknown, which significantly hinders the development of effective immunotherapies for these lethal malignancies.

Paradoxically, SCLC contains a high tumor mutation burden (TMB) but is a typical immune-desert tumor.[13,14] Recently, emerging evidence suggested that tumor vasculature, formed through aberrant angiogenesis and exhibiting structural and functional abnormalities, might have a profound influence on the TME. Though tumor vessels are typically disorganized, leaky, and inefficient, they can selectively regulate the entry of immune cells. For example, endothelial cells can help T cells arrest and infiltrate by expressing adhesion molecules.[15–18] Primary and metastatic tumors in the brain, which are generally immune cold and respond poorly to immunotherapies, possess a unique blood-tumor barrier (BTB) against the immune cell infiltration.[19–21] In this study, we demonstrate that unprecedented blood-brain barrier-like vascular gates (BVGs) are prevalent in NECs, potentially contributing to their immune exclusion properties and limited immunotherapy response.

RESULTS

An unusual vasculature associated with immunosuppression in SCLC

Immunotherapies show varying efficacy in different human cancers, and among them, SCLC and glioblastoma (GBM) display the poorest response, as evidenced by their minimal overall survival (OS) benefit and low objective response rates (ORRs) in clinical trials (Figure 1A; Table S1). Consistent with this observation, SCLC exhibits the second-lowest T cell infiltration after GBM in pan-cancer analyses, a feature that likely contributes to its resistance to immune checkpoint inhibitors (ICIs) (Figure 1B; Table S1). Transcriptomics analyses of multiple ICI-treated pan-cancer cohorts ($n = 413$)[22–33] revealed that multiple vasculature-related pathways, including endothelial cell morphology, vascular smooth muscle cell development, and endothelial brain barrier pathways, showed significant negative correlations with T cell infiltration (Figure 1C). Further, the immune-excluded ASCL1$^+$ and NEUROD1$^+$ subtypes exhibited markedly reduced T cell infiltration compared to inflammatory subtypes. These subtypes were also strongly associated with vascular permeability/tight junction interaction gene signatures in SCLC (Figure 1D). OpenTSNE visualization confirmed significantly fewer immune cells in SCLC than in non-SCLC (NSCLC) (Figure S1A; Table S2). Specifically, the proportions of infiltrating T cells, B cells, and macrophages were lower in SCLC than in NSCLC (Figure S1B). Notably, endothelial cells in SCLC displayed the highest number of differentially expressed genes (DEGs) among TME populations (Figure 1E). These DEGs included multiple basement membrane-associated genes (e.g., *NID1*, *COL4A1*, and laminin-related genes), which were either absent or expressed at much lower levels in NSCLC endothelium (Figure S1C). Pathway analysis further revealed enrichment of extracellular matrix (ECM) and basement membrane-related pathways in SCLC endothelial cells compared to controls (Figure 1F). Together, these findings suggest that SCLC vasculature possesses distinct molecular properties, potentially contributing to its immune-excluding phenotype and poor immunotherapy response.

To directly visualize the features of SCLC vasculature, we conducted histopathological analyses of human SCLC tissues and used NSCLC as a control. Hematoxylin and eosin (H&E) staining demonstrated that SCLC vessels exhibited endothelial cells arranged in a highly organized pattern, surrounded by an abnormally thick basement membrane. In contrast, NSCLC displayed disorganized endothelial cells with thin basement membranes (Figure 1G). Transmission electron microscopy (TEM) further corroborated these findings, revealing a dense basement membrane enveloping SCLC endothelial cells. Notably, SCLC vasculature exhibited frequent tight junctions between endothelial cells, along with robust pericyte coverage—features that were largely absent in NSCLC (Figure 1H). To molecularly define these structural aberrations, we performed immunofluorescence (IF) staining. Consistent with H&E and TEM results, SCLC vessels showed strong expression of basement membrane components (collagen IV and laminin) compared to NSCLC. Moreover, zonula occludens-1 (ZO-1), a key tight junction protein, was selectively detected in SCLC endothelium but not in NSCLC. Additionally, pericyte markers, alpha-smooth muscle actin(αSMA) and platelet-derived growth factor receptor beta (PDGFRβ), were highly expressed around SCLC vessels, indicating extensive pericyte ensheathment, whereas NSCLC exhibited minimal staining (Figures 1I and S1D). Collectively, these data demonstrate that SCLC vasculature is structurally distinct, characterized by a thickened basement membrane, prominent tight junctions, and dense pericyte coverage, blood-brain barrier (BBB)-like features that may contribute to its immune-excluding phenotype.

Murine SCLC models exhibit aberrant vasculature mirroring human disease

To investigate the biology of SCLC vasculature, we established mouse models by orthotopically transplanting *Trp53*$^{-/-}$, sg*Rb1*, *Myc*, and Cas9 premalignant lung organoids, using our recently developed genetically engineered organoid-initiated mouse model (GEOMM) platform.[34] These animals developed aggressive tumors within 2–3 months (Figure S2A). Histopathological analysis confirmed that these tumors represented classic ASCL1$^+$ SCLC, mirroring the features observed in established genetically engineered mouse models (GEMMs) of SCLC[35,36] (Figures S2B and S2C). Notably, multiplex immunohistochemistry (mIHC) staining revealed minimal T cell infiltration in these murine SCLCs, a striking contrast to NSCLC models,[37] thereby recapitulating the immune-desert phenotype characteristic of human SCLC (Figures S2D and S2E). Together, these data demonstrate that our SCLC GEOMMs faithfully replicate the immunosuppressive TME seen in human SCLC.

Please cite this article in press as: Wang et al., A blood-brain barrier-like vascular gate limits immunotherapy efficacy in neuroendocrine cancers, Cell (2026), https://doi.org/10.1016/j.cell.2026.04.017

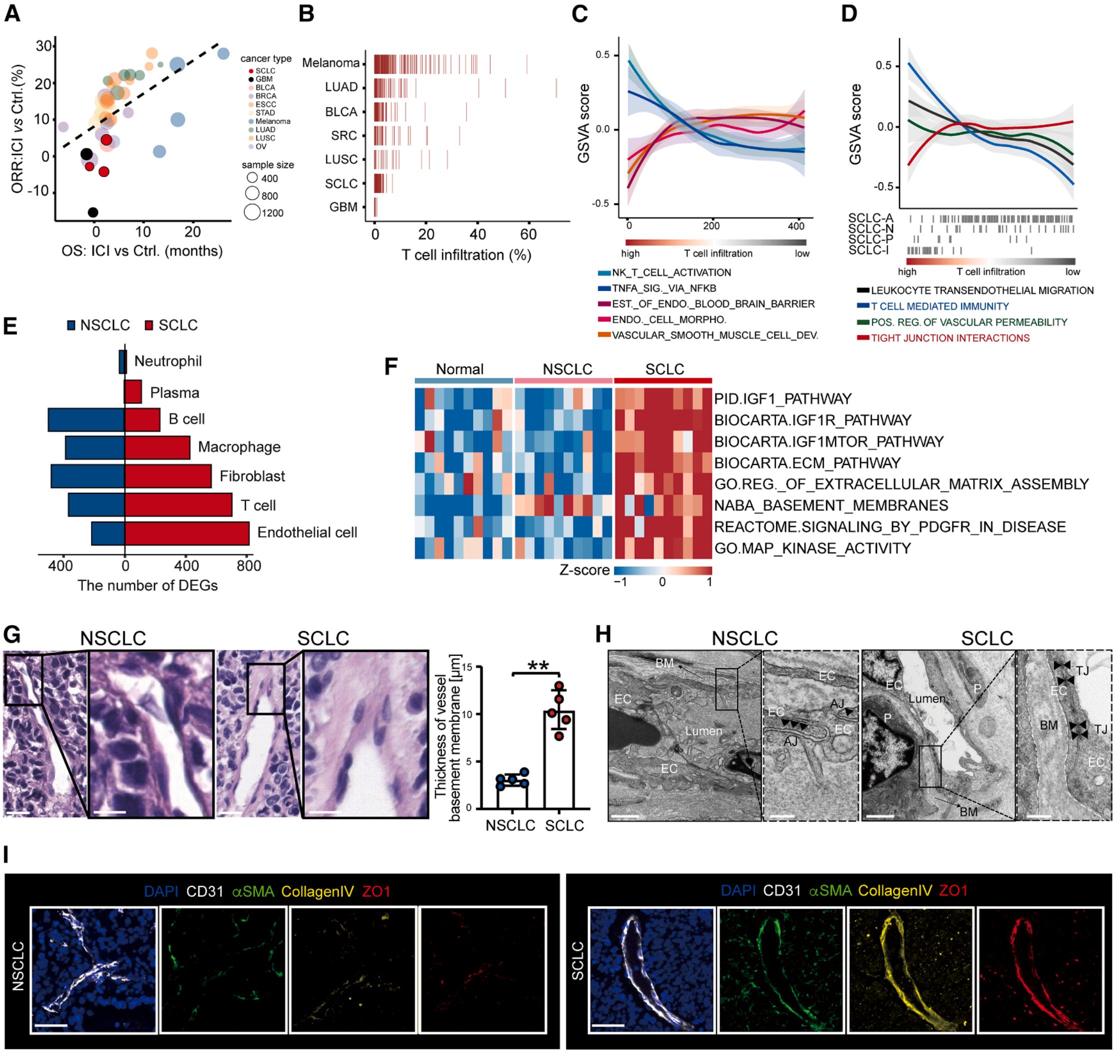

Figure 1. SCLC vasculature coinciding with immunosuppression shows basement-membrane thickening and tight-junction enrichment

(A) The scatter plot illustrates the benefit of OS and ORR in patients receiving immune checkpoint blockade therapy. The circle size represents the number of patients included in each cohort, and the colors indicate different tumor types.

(B) Proportion of T cell infiltration across tumor types in pan-cancer immune checkpoint blockade cohorts. Each red line represents one patient. T cell infiltration was estimated by deconvolution analysis of RNA-seq data from bladder urothelial carcinoma (BLCA) (n = 171), lung adenocarcinoma (LUAD) (n = 124), lung squamous cell carcinoma (LUSC) (n = 44), melanoma (n = 404), SCLC (n = 163), glioblastoma (GBM) (n = 34), and sarcoma (n = 87) patients.

(C) Gene set variation analysis (GSVA) scores for natural killer T (NKT) cell activation, tumor necrosis factor α (TNF-α) signaling, endothelial morphogenesis, and endothelial barrier function pathways are shown according to T cell infiltration levels across pan-cancer immune checkpoint blockade cohorts. T cell infiltration was estimated by RNA-seq deconvolution in BLCA (n = 89), LUAD (n = 113), LUSC (n = 41), melanoma (n = 114), SCLC (n = 18), and sarcoma (n = 38) patients.

(D) GSVA scores for leukocyte trans-endothelial migration, T cell-mediated immunity, positive regulation of vascular permeability, and tight junction (TJ) interaction pathways are shown by T cell infiltration level in the SCLC immune checkpoint blockade cohort from the IMpower133 trial.

(E) Number of DEGs across cell types in NSCLC and SCLC tumors, based on single-cell transcriptomic data from Chan et al.[6]

(F) Upregulated pathways in SCLC ECs compared with ECs from normal tissues and NSCLC tumors, based on single-cell transcriptomic data from Chan et al.[6]

(G) Representative H&E staining of paraffin-embedded NSCLC (left) and SCLC (right) patient tumors. Scale bars, 20 μm, magnified region, 10 μm. Bar plots quantify the average thickness of the BM in tumor blood vessels. Mean ± SD (n = 5). $^{**}p < 0.01$. Mann-Whitney test.

(H) TEM images of tumor blood vessels in patient NSCLC (left) and SCLC (right) samples. EC, endothelial cell; AJ, adherens junction; BM, basement membrane; TJ, tight junction; and P, pericyte. Scale bars, 1 μm, magnified region, 250 nm.

(I) Consecutive sections of patient NSCLC (left) and SCLC (right) tumors were analyzed by IF for the expression of CD31, αSMA, collagen IV, and ZO-1, as described in STAR Methods. Scale bars, 50 μm.

See also Figure S1.

Please cite this article in press as: Wang et al., A blood-brain barrier-like vascular gate limits immunotherapy efficacy in neuroendocrine cancers, Cell (2026), https://doi.org/10.1016/j.cell.2026.04.017

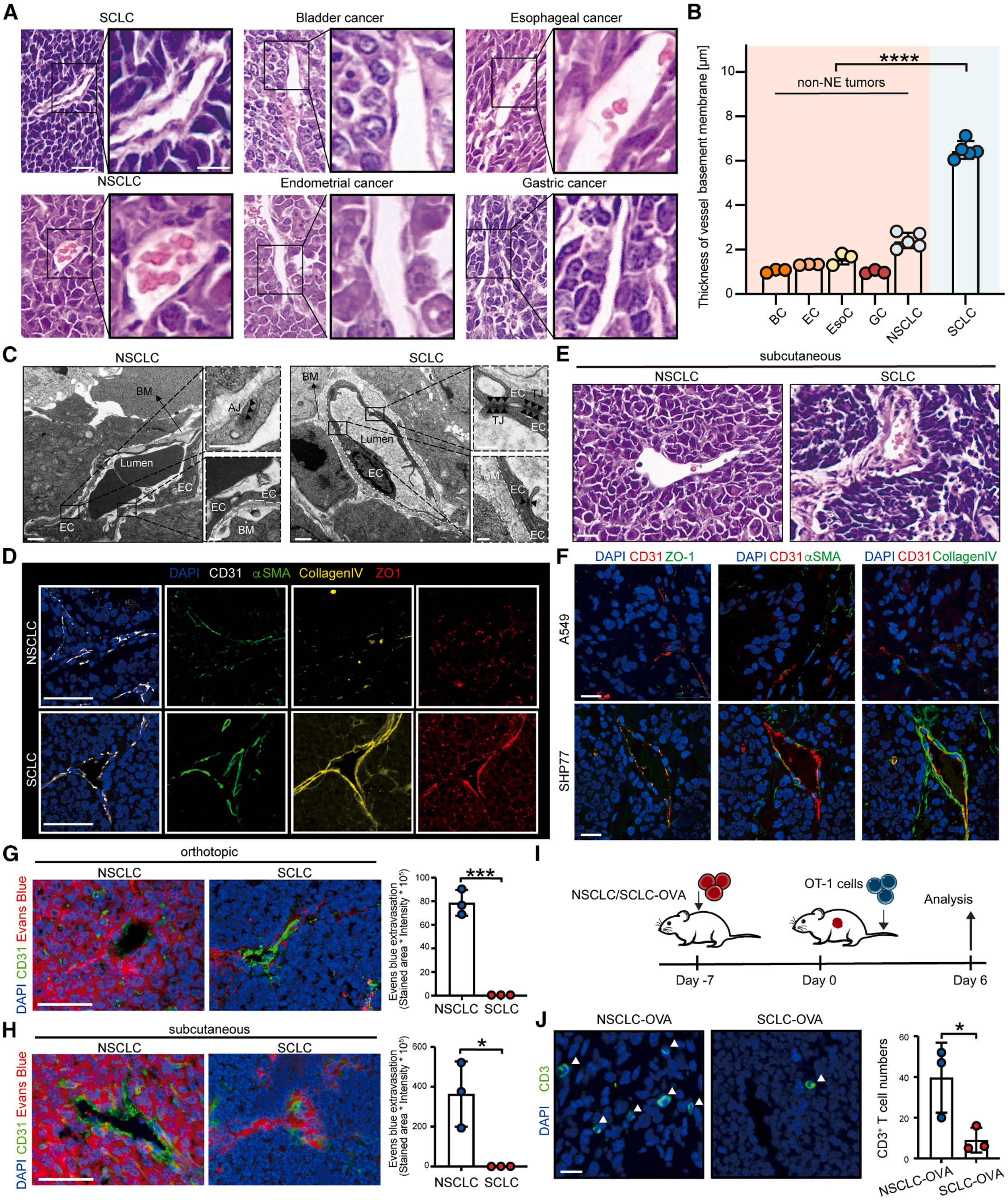

Figure 2. The SCLC-BVG is induced by tumor cells and prevents T cell infiltration

(A and B) Representative H&E staining images of paraffin-embedded mouse tumor samples from NSCLC, esophageal cancer (EsoC), endometrial cancer (EC), gastric cancer (GC), bladder cancer (BC), and SCLC. Scale bars, 20 μm, magnified region, 10 μm (A). Quantification of the average thickness of tumor blood vessels in each tumor type (B). Mean ± SD ($n_{NSCLC} = 5$; $n_{EsoC} = 3$; $n_{EC} = 3$; $n_{GC} = 3$; $n_{BC} = 3$; $n_{SCLC} = 5$). ****$p < 0.0001$. Mann-Whitney test.

(C) TEM images of tumor blood vessels in mouse NSCLC (left) and SCLC (right) samples. EC, endothelial cell; AJ, adherens junction; BM, basement membrane; TJ, tight junction; and P, pericyte. Scale bars, 1 μm, magnified region, 250 nm.

(D) Consecutive sections of mouse NSCLC (top) and SCLC (bottom) tumor samples were analyzed by IF for the expression of CD31, αSMA, collagen IV, and ZO-1, as described in STAR Methods. Scale bars, 50 μm.

(E) Representative H&E staining of paraffin-embedded samples from mouse subcutaneous NSCLC and SCLC tumors. Scale bars, 20 μm.

(F) Consecutive sections of tumor from nude mice injected with A549 or SHP77 human cell lines were analyzed by IF for the expression of CD31, ZO-1, αSMA, and collagen IV. Scale bars, 20 μm.

(G and H) Representative images of CD31 staining and Evans Blue dye in mouse NSCLC (left) and SCLC (right) orthotopic (G) and subcutaneous (H) tumors. Scale bars, 50 μm. Bar plots show quantification of tumor blood vessel permeability. Mean ± SD ($n = 3$). *$p < 0.05$, ***$p < 0.001$. *t* test.

(legend continued on next page)

Please cite this article in press as: Wang et al., A blood-brain barrier-like vascular gate limits immunotherapy efficacy in neuroendocrine cancers, Cell (2026), https://doi.org/10.1016/j.cell.2026.04.017

We next investigated whether these murine SCLCs recapitulated the abnormal vasculature observed in patients. H&E staining revealed that SCLC vessels were enveloped by an abnormally thick basement membrane, whereas NSCLC and other non-NECs, including esophageal cancer, endometrial cancer, gastric cancer, and bladder cancer, exhibited thinner basement membranes[38–41] (Figures 2A and 2B). TEM further confirmed these structural aberrations, demonstrating dense basement membranes, frequent endothelial tight junctions, and complete pericyte coverage in SCLC—features absent in NSCLC controls (Figure 2C). IF staining validated these findings, showing strong expression of basement membrane components (collagen IV, laminin), the tight junction protein ZO-1, and pericyte markers (αSMA, PDGFRβ) in SCLC vasculature (Figures 2D and S2F). Thus, murine SCLCs phenocopy the aberrant vascular architecture of human SCLC—thickened basement membranes, reinforced tight junctions, and robust pericyte coverage—features likely contributing to their immune-excluding phenotype.

SCLC tumor cells induce a BVG

Given that murine SCLC and NSCLC share the same organ microenvironment yet exhibit distinct vascular architectures, we hypothesized that SCLC tumor cells actively drive the formation of these abnormal vessels. To test this, we subcutaneously transplanted murine SCLC or NSCLC cells into recipient mice. Histological analysis revealed that subcutaneous SCLC tumors recapitulated the aberrant vascular features observed in orthotopic lung tumors, including an abnormally thick basement membrane surrounding the vessels (Figure 2E). We extended these findings to human models using the SCLC cell line SHP77 and the A549 lung adenocarcinoma line as a control. All cell lines formed subcutaneous tumors in nude mice. IF staining demonstrated that the SHP77 tumors, but not the A549 controls, exhibited vascular structures with thick basement membranes (high collagen IV), prominent tight junctions (ZO-1), and dense pericyte coverage (αSMA) (Figure 2F). These results establish that SCLC tumor cells autonomously induce the formation of this unique vasculature, independent of their organ microenvironment.

The structural features of SCLC vasculature suggested barrier-like properties. To evaluate this functionally, we performed vascular permeability assays. In orthotopic models, Evans' blue dye readily extravasated in NSCLC tumors but was confined to vessels in SCLC, mimicking the BBB (Figure 2G). Subcutaneous SCLC tumors similarly restricted dye leakage, confirming that this phenotype is tumor cell-driven (Figure 2H). To directly test the immune cell exclusion function of SCLC vessels, we transplanted ovalbumin (OVA)-expressing NSCLC and SCLC cells into nude mice, followed by perfusion with OT-1 T cells (Figure 2I). The results showed significantly lower T cell infiltration in SCLC compared to NSCLC (Figure 2J). These data demonstrate that SCLC tumor cells induce a specialized vasculature characterized by structural barriers with thick basement membranes, tight junctions, and pericytes, and functional properties of immune cell exclusion. Consistently, anti-programmed cell death protein 1 (anti-PD1) treatment significantly prolonged survival in NSCLC-bearing mice but showed minimal efficacy in SCLC models (Figure S2G).

Since vascular architecture may also influence blood flow and pH, we wondered whether these unique vessels would affect blood flow and pH in SCLC. Doppler ultrasound showed that the peak velocity of blood flow within the SCLC tumors was significantly higher than that in the NSCLC tumors (Figure S2H). Consistently, a lectin perfusion assay[42,43] confirmed that most of the SCLC vessels had active blood flow, compared with only about 20% in NSCLC tumors (Figure S2I). Then we assessed intratumoral pH by seminaphthorhodafluor-4F 5-(and-6)-carboxylic acid (SNARF-4F) staining[44] and observed no significant difference between SCLC and NSCLC (Figure S2J). Thus, the SCLC vessels had increased blood flow but no obvious effect on intratumoral pH. Taken together, we propose the term BVG to describe this SCLC-specific vascular phenotype, which might mechanistically contribute to the immune-desert TME and immunotherapy resistance.

ASCL1 is essential for the BVG structure of SCLC

To investigate the molecular characteristics underlying the BVG structures in SCLC, we performed transcriptomic analyses on endothelial cells isolated from NSCLC and SCLC. The top upregulated genes in SCLC endothelial cells were enriched in pathways related to the basement membrane, tight junctions, and specifically, the endothelial barrier gene signature (Figures 3A, 3B, S3A, and S3B; Tables S3 and S4). To validate these findings at the protein level, we utilized microdissection and hydrogel-based expansion-mass spectrometry to analyze vessels from SCLC and NSCLC. Consistent with the transcriptomic data, protein levels of endothelial barrier-associated genes and pathways were significantly upregulated in SCLC vessels (Figures 3C, 3D, S3C, and S3D; Tables S3 and S4). Importantly, these endothelial barrier-related pathways were similarly upregulated in endothelial cells from SCLC compared to those of NSCLC, pan-cancers, or normal lung tissues (Figure 3E; Table S3). These findings further confirmed the barrier-like properties of SCLC vessels.

By comparing the transcriptomic profiles of SCLC endothelial cells with those from normal lung, NSCLC, and pan-cancer endothelial cells, we derived a SCLC-BVG gene signature consisting of 1,279 genes (Figure S3E; Table S4). The BVG signature was significantly negatively associated with infiltration of T cells upon immunotherapy in the Impower133 cohort (Figure S3F). More importantly, SCLC patients with a high BVG signature had significantly worse progression-free survival (PFS) with immunotherapy than those with a low BVG signature, whereas no significant difference in PFS was observed in the placebo group (Figure 3F). Given the critical role of tumor cells in driving the formation of BVG

(I) Scheme of the OT-1 T cell infiltration assay. OVA-expressing NSCLC or SCLC cells were subcutaneously inoculated into nude mice, and OT-1 T cells were adoptively transferred via tail vein injection to assess tumor infiltration.

(J) Representative IF staining images of CD3 in OVA-expressing NSCLC and SCLC tumors after adoptive transfer of OT-1 T cells. Scale bars, 20 μm. Bar plot quantifies infiltrating T cells. Mean ± SD ($n = 3$). $^*p < 0.05$. t test.

See also Figure S2.

Please cite this article in press as: Wang et al., A blood-brain barrier-like vascular gate limits immunotherapy efficacy in neuroendocrine cancers, Cell (2026), https://doi.org/10.1016/j.cell.2026.04.017

structures in SCLC (Figure 2E), we ranked SCLC-specific genes by their correlation with the SCLC-BVG gene signature. Interestingly, most of these genes showed a positive correlation, with ASCL1—a defining marker of the classic neuroendocrine subtype of SCLC—ranking at the top (Figures S3G and S3H; Table S4). *ASCL1*$^+$ SCLC exhibited the most pronounced barrier-like features, compared to other non-*ASCL1*$^+$ SCLC subtypes (Figures 3G and S3I; Table S4). Whereas *ASCL1*$^+$ SCLC tumors (SCLC-A) are immune-desert and have poor response to immunotherapy, the inflamed SCLC (SCLC-I) tumors can significantly benefit from immunotherapy.[8] Thus, we wondered whether these two subtypes of SCLC would have differences in terms of the BVG structures. The expression levels of the BVG signature genes were significantly higher in SCLC-A tumors than in SCLC-I tumors (Figure 3H). To more accurately dissect the BVG features, we performed single-cell RNA sequencing (scRNA-seq) analyses of tumor samples from 10 SCLC patients, including 7 SCLC-A and 3 SCLC-I (Figure S3J; Table S5). And consistently, the BVG signature was significantly increased in the endothelial cells of SCLC-A tumors than those of SCLC-I tumors (Figure S3K). Further, histopathology confirmed the existence of BVG in SCLC-A tumors but not in the SCLC-I ones (Figure S3L). These data indicate that the BVG signature is a unique feature of SCLC-A tumors and is associated with poor response to immunotherapy. Specifically, several basement membrane-associated genes (*COL4A1*, *COL4A2*, *NID1*, *LAMB1*, *LAMC1*, and *LAMA4*) are highly expressed in endothelial cells from *ASCL1*^{high} SCLC patients (Figure 3I).[6,9,45]

ASCL1 is not only a marker but also a master regulator of SCLC.[46–48] We wondered whether ASCL1 also governs the BVG structures in SCLC. Supporting this hypothesis, the loss of *Ascl1* in tumor cells significantly reduced basement membrane thickness and decreased the expression of collagen IV and laminin. Tumors lacking *Ascl1* also showed diminished expression of αSMA, PDGFRβ, and ZO-1, indicated by reduced pericyte coverage and tight junctions compared to control SCLC (Figures 3J, 3K, and S3M). Additionally, *ASCL1*$^+$ SCLC demonstrated more immune suppression than non-neuroendocrine (NE) SCLC subtypes, characterized by reduced T cell infiltration (Figure 3L; Table S4). Notably, the disruption of BVG structures caused by *Ascl1* loss increased CD8$^+$ T cell infiltration in SCLC (Figure 3M). Collectively, these findings establish *ASCL1* as a key regulator of the BVG structures in SCLC.

The SCLC tumor cells induce BVG structures through the ASCL1-IGFBP5-IGF1R axis

To investigate the molecular mechanism by which ASCL1 regulates the formation of BVG structures in SCLC, we ranked ASCL1's direct downstream target genes[49] based on their correlation with the SCLC-BVG gene signature (Figures 4A and S4A; Table S4). Among the top candidates, we focused on insulin-like growth factor-binding protein 5 (IGFBP5). IGFBP5 was highly expressed in human and mouse SCLC, particularly in *ASCL1*$^+$ NE tumors,[50] but not in NSCLC (Figures 4B and S4B–S4D). *IGFBP5* expression levels were significantly correlated with those of *ASCL1* and the BVG gene signature in SCLC patients (Figures S4E and S4F). ASCL1 loss led to reduced IGFBP5 expression both *in vitro* and *in vivo* (Figures 4C and S4G).

Strikingly, the BVG structures were completely abolished in *Igfbp5*-deficient SCLC (Figure 4D). TEM revealed reductions in basement membrane thickness and tight junctions in these vessels (Figure 4E). And the expression levels of collagen IV, laminin, αSMA, PDGFRβ, and ZO-1 were significantly decreased in *Igfbp5*-deficient SCLC (Figures 4F and S4H). Moreover, the Evans Blue assay demonstrated increased vascular permeability in *Igfbp5*-deficient SCLC (Figure 4G). This loss of barrier-like features was accompanied by a significant increase in T cell infiltration (Figure 4H). Transcriptomic and proteomic analyses further confirmed a substantial reduction in the BVG gene signature in endothelial cells from *Igfbp5*-deficient SCLC (Figures 4I and S4I; Table S2). These results demonstrate that IGFBP5, downstream of ASCL1, is essential for the formation of BVG structures in SCLC.

IGFBP5 binds and transports insulin-like growth factor 1(IGF1) to target cells.[51,52] Both scRNA-seq and spatial proteomics analyses revealed a significant reduction in IGF1/IGF1 receptor (IGF1R) signaling in endothelial cells from *Igfbp5*-deficient SCLC (Figure 4J). Multiplex IHC further confirmed decreased IGF1 and IGF1R levels in *Igfbp5*-deficient SCLC (Figure 4K). To assess the functional relevance of the IGF1R signaling pathway, endothelial cells with or without *Igf1r* disruption were co-transplanted with SCLC tumor cells into mice (Figure 4L). In tumors containing *Igf1r*-deficient endothelial cells, BVG structures were absent (Figures 4M and S4J). There was increased permeability and significantly increased T cell infiltration (Figure 4N). Consistent with the mouse model, we observed significantly increased levels of IGFBP5 at both RNA and protein levels, IGF1/IGF1R signature scores, and IGF1/IGF1R pathway phosphorylation in ASCL1^{high} SCLC patients, as analyzed in the published Tongji University [TU]-SCLC cohort (Figure 4O).[9] Together, these findings reveal that the ASCL1-IGFBP5-IGF1R axis mediates the induction of BVG structures by SCLC tumor cells.

ASCL1 and IGFBP5 are sufficient to induce the BVG structure

To test whether ASCL1 and IGFBP5 are sufficient to induce the BVG structure, we overexpressed ASCL1 and IGFBP5 in H526 cells, a validated ASCL1$^-$ POU2F3$^+$ SCLC cell line, and then transplanted them into nude mice (Figure S5A). IF staining showed that forced ASCL1 expression significantly increased the expression of IGFBP5 in H526 cells, whereas overexpressing IGFBP5 in H526 cells did not have a significant effect on the expression of ASCL1 (Figures 5A–5C). And strikingly, we observed dramatically altered morphology of blood vessels, characterized by a surrounding thick basement membrane and dense pericytes, in both ASCL1 and IGFBP5-overexpressed tumors. IF staining confirmed the significantly increased αSMA$^+$ vessels in the ASCL1 and IGFBP5-overexpressed tumors but not in the control (Figures 5D–5G). Thus, ASCL1 and IGFBP5 are sufficient to induce the BVG structure in non-NE SCLC tumors.

Further, we tested whether ASCL1 and IGFBP5 were sufficient to induce the BVG structure even in NSCLC. We ectopically expressed ASCL1 or IGFBP5 in mouse NSCLC organoids[37] and then transplanted them into C57BL/6 recipients. Histopathological assays revealed that a BVG-like structure was present in

Please cite this article in press as: Wang et al., A blood-brain barrier-like vascular gate limits immunotherapy efficacy in neuroendocrine cancers, Cell (2026), https://doi.org/10.1016/j.cell.2026.04.017

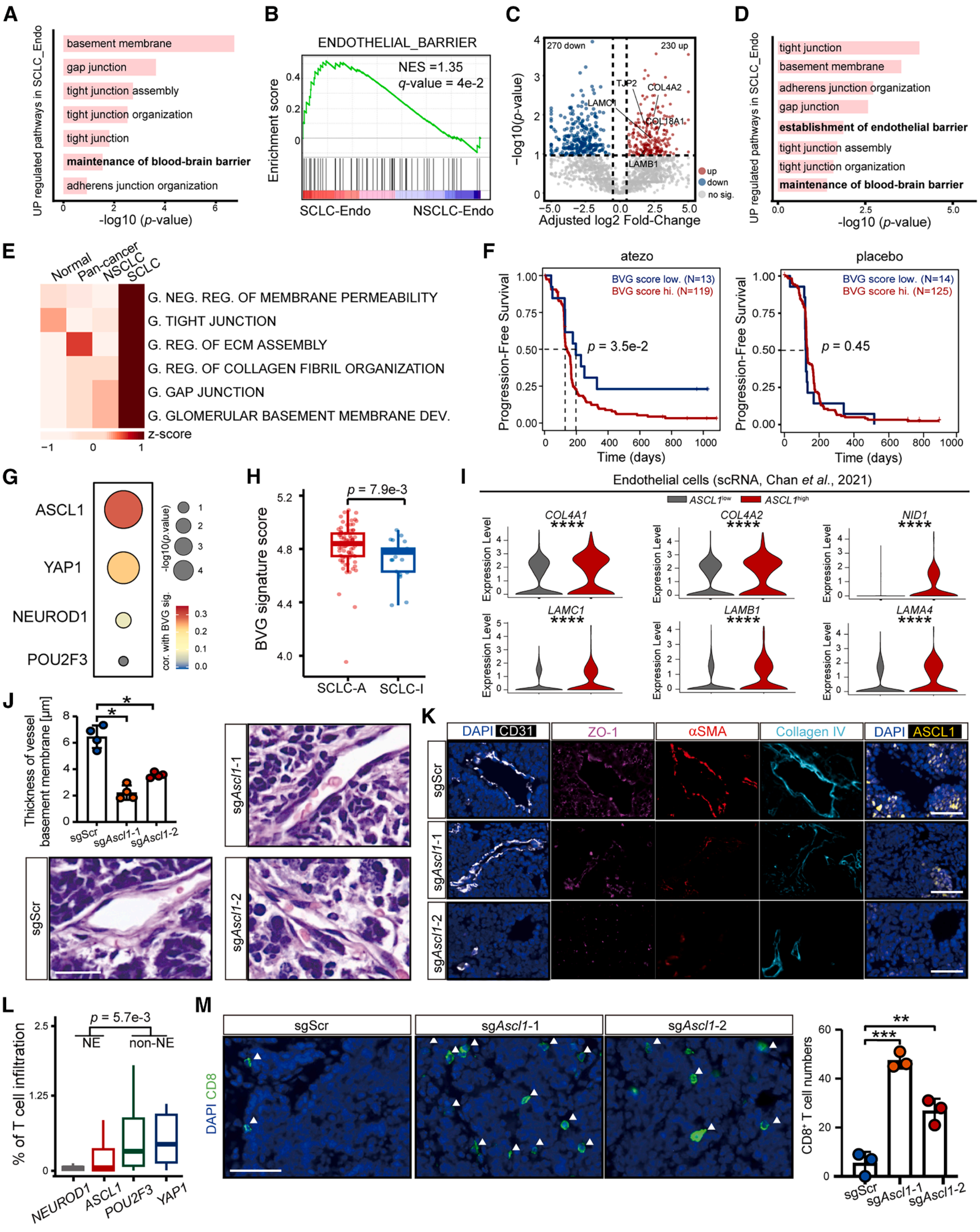

Figure 3. ASCL1 is essential for the BVG

(A) Gene Ontology analysis identified pathways enriched in upregulated genes in mouse-derived SCLC ECs compared to NSCLC-derived ECs.

(B) Gene set enrichment analysis (GSEA) revealed significant positive enrichment of the ENDOTHELIAL_BARRIER in mouse-derived SCLC ECs compared to NSCLC ECs.

(C) Volcano plot of differentially abundant proteins in tumor vascular regions from mouse SCLCs versus NSCLCs. Differentially abundant proteins were defined by $p < 0.1$ and absolute adjusted $\log_2$ fold-change > 0.5. Tight junction- and BM-associated proteins are highlighted.

(D) Gene Ontology analysis of proteins increased in vascular regions of mouse SCLC versus NSCLC.

(E) Upregulated pathways in SCLC-derived ECs ($n = 524$ cells) relative to ECs from normal lung tissues ($n = 7{,}921$ cells), lung adenocarcinoma ($n = 2{,}369$ cells), and pan-cancer tumors (bladder, $n = 5{,}423$ cells; breast, $n = 7{,}605$ cells; colorectal, $n = 1{,}515$ cells; esophageal, $n = 207$ cells; osteosarcoma, $n = 2{,}655$ cells;

(legend continued on next page)

Please cite this article in press as: Wang et al., A blood-brain barrier-like vascular gate limits immunotherapy efficacy in neuroendocrine cancers, Cell (2026), https://doi.org/10.1016/j.cell.2026.04.017

both ASCL1 and IGFBP5-overexpressed NSCLC tumors, but not in the control ones (Figures 5H–5K). Following these observations, we analyzed lung adenocarcinoma (LUAD) patients from The Cancer Genome Atlas (TCGA) to explore the potential clinical relevance of ASCL1 and IGFBP5 aberrant expressions and the BVG structure (Table S6). The results showed that, whereas most NSCLC tumors expressed very low levels of ASCL1 and IGFBP5, 11 out of 594 patients were ASCL1$^+$. And these ASCL1$^+$ patients also expressed high levels of IGFBP5 (Figures S5B and S5C). Of note, they displayed significantly higher BVG signature (Figure S5D). And the H&E slides of these patients showed BVG-like structures (Figure S5E). These data indicate that ASCL1 and IGFBP5 are sufficient to induce BVG-like structures in even NSCLC tumors, which might occur in patients.

Targeting the ASCL1-IGFBP5-IGF1R axis enhances immunotherapy efficacy in SCLC

Given the critical role of the ASCL1-IGFBP5-IGF1R axis in maintaining BVG structures that limit T cell infiltration in SCLC, we investigated whether targeting this axis could improve the efficacy of immunotherapy. Control and *Igfbp5*-deficient SCLC tumor cells were transplanted into C57BL/6 mice, followed by treatment with either vehicle or anti-PD1 antibodies (Figure 6A). Whereas *Igfbp5* loss had no effect on tumor cell growth *in vitro*, it moderately reduced tumor growth *in vivo*, suggesting an influence mediated by the TME (Figures 6B and S6A). Remarkably, anti-PD1 antibody treatment completely suppressed the growth of *Igfbp5*-deficient tumors but had minimal impact on control tumors (Figure 6B). Multiplex IHC analysis revealed that *Igfbp5*-deficient tumors, which exhibited impaired BVG structures, showed increased infiltration of CD8$^+$ T cells. Although anti-PD1 treatment alone did not significantly alter CD8$^+$ T cell infiltration, it dramatically enhanced infiltration in *Igfbp5*-deficient tumors (Figures 6C, 6D, and S6B–S6D; Table S2). These findings indicate that disrupting BVG structures can synergize with immunotherapy to enhance its efficacy in SCLC.

Within this axis, IGF1R inhibitors have been developed and shown clinical safety.[53–57] One of them, linsitinib (OSI-906), was tested in a phase II clinical trial for SCLC patients but showed no significant clinical benefit as a standalone treatment.[58] Consistently, OSI-906 monotherapy only moderately slowed SCLC growth in mice. However, the combination of OSI-906 with anti-PD1 antibodies markedly suppressed SCLC progression (Figures 6E and 6F). Mechanistically, OSI-906 treatment significantly reduced the basement membrane thickness of SCLC-associated vessels (Figures S6E and S6F). OSI-906 treatment alone slightly increased immune cell infiltration, whereas its combination with anti-PD1 antibodies significantly elevated CD8$^+$ T cell numbers and the proportion of various immune cells, as shown by multiplex IHC and scRNA-seq analyses (Figures 6G–6I; Table S2). It also markedly enhanced interactions between tumor cells and T cells (Figure S6G). In addition, marker genes associated with T cell cytotoxicity, stem-like/memory potential, migratory/infiltrative capacity, and proliferative/survival programs were upregulated by *Igfbp5* knockout or OSI-906 treatment (Figure S6H). Moreover, previous studies suggested that there were immunosuppressive monocytes and macrophages in SCLC,[6] and we found that OSI-906 treatment by itself or combined with immune checkpoint blockade (ICB) dramatically reduced these populations (macro-c1) while increasing those with enhanced anti-tumor activities (macro-c0 and -c2) (Figures S6I–S6K). Of note, OSI-906 treatment slightly slowed blood flow, as indicated by Doppler ultrasound and a lectin perfusion assay, but had no significant effect on intratumoral pH of SCLC (Figures S6L–S6N). Collectively, these results indicated that disrupting BVG increased the infiltration of immune cells and their anti-tumor activity in SCLC.

These results further validate the function of the ASCL1-IGFBP5-IGF1R in the BVG structures and the immunosuppressive feature, and highlight the therapeutic potential of targeting the axis to enhance immunotherapy efficacy in SCLC.

The presence of BVG structures in pan-NE tumors

Given the resemblance of other NE tumors to SCLC, we investigated whether the BVG structures identified in SCLC also exist in pan-NE tumors. Histopathological analyses revealed that several NE tumors, including esophageal NEC (Eso-NEC), bladder NEC (BL-NEC), gastric NEC (Gas-NEC), pancreatic NEC (P-NEC), rectal NEC (RE-NEC), and castration-resistant

---

ovarian, $n = 3{,}268$ cells; prostate, $n = 1{,}227$ cells; hepatocellular carcinoma, $n = 262$ cells; lung squamous cell carcinoma, $n = 720$ cells; melanoma, $n = 1{,}353$ cells; renal cell carcinoma, $n = 4{,}211$ cells; gastric, $n = 8{,}242$ cells).

(F) Progression-free survival of SCLC patients treated with chemotherapy plus immunotherapy (left) or chemotherapy (right), stratified by high and low BVG scores in the IMpower133 cohort.[33] p values were calculated using the log-rank test.

(G) Correlation of *ASCL1*, *NEUROD1*, *YAP1*, and *POU2F3* expression with the BVG signature in SCLC cohorts. Reanalyzed RNA-seq data from Liu et al.[9] and George et al.[45] ($n = 194$).

(H) BVG signature levels in immunotherapy-treated SCLC-A ($n = 77$) and SCLC-I ($n = 21$) patients, based on IMpower133 transcriptomic data.[33] p values were calculated by a two-sided Wilcoxon rank-sum test.

(I) Basement membrane-associated gene expression in ECs from $ASCL1^{low}$ ($n = 28$ patients) and $ASCL1^{high}$ ($n = 13$ patients) lung cancer samples, based on reanalyzed scRNA-seq data from Chan et al.[6] $^{****}p < 0.0001$. Two-sided Wilcoxon rank-sum test.

(J) Representative H&E staining of paraffin-embedded mouse SCLC tumors genetically edited with sgScr and sg*Ascl1*. Scale bars, 20 μm. Bar plots quantify the average thickness of the BM in tumor blood vessels. Mean ± SD ($n = 4$). $^{*}p < 0.05$. Mann-Whitney test.

(K) Consecutive sections of mouse SCLC tumors edited with sgScr and sg*Ascl1* were analyzed by IF for the expression of ASCL1, CD31, αSMA, collagen IV, and ZO-1, as described in STAR Methods. Scale bars, 50 μm.

(L) T cell infiltration levels across SCLC subtypes: SCLC-A ($n = 149$), SCLC-N ($n = 15$), SCLC-P ($n = 22$), and SCLC-Y ($n = 8$) patients. RNA-seq data were reanalyzed from Liu et al.[9] and George et al.[45] Two-sided Wilcoxon rank-sum test.

(M) IF analysis of CD8 in mouse SCLC tumors edited with sgScr or sg*Ascl1*. Scale bars, 50 μm. Bar plot shows the quantification of infiltrating T cells. Mean ± SD ($n = 3$). $^{**}p < 0.01$. $^{***}p < 0.001$, t test.

See also Figure S3.

Please cite this article in press as: Wang et al., A blood-brain barrier-like vascular gate limits immunotherapy efficacy in neuroendocrine cancers, Cell (2026), https://doi.org/10.1016/j.cell.2026.04.017

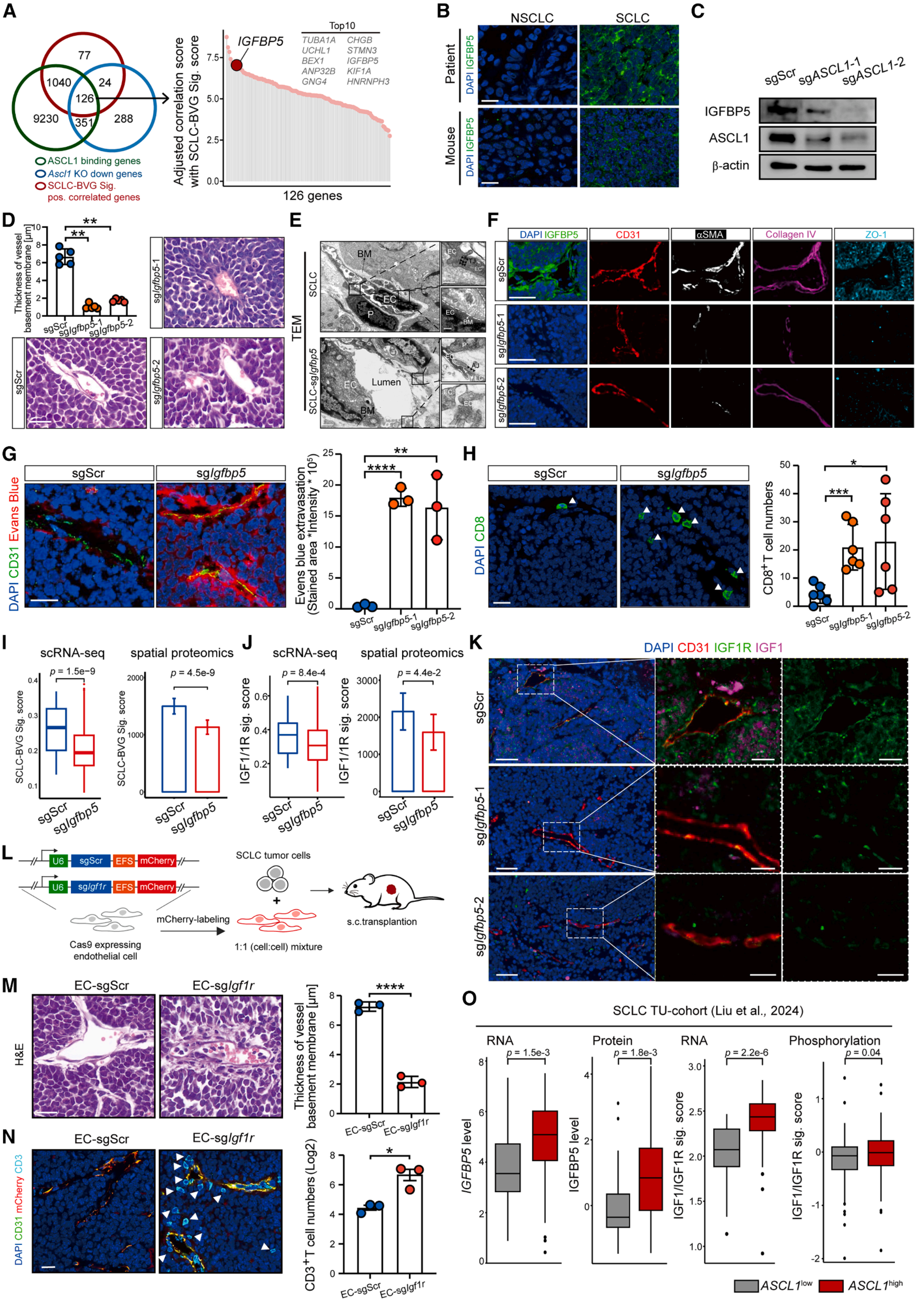

(legend on next page)

Please cite this article in press as: Wang et al., A blood-brain barrier-like vascular gate limits immunotherapy efficacy in neuroendocrine cancers, Cell (2026), https://doi.org/10.1016/j.cell.2026.04.017

neuroendocrine prostate cancer (CRPC-NE), exhibited BVG structures characterized by a thick basement membrane, a feature absent in non-NE tumors (Figures 7A and 7B). IF staining further confirmed high expression levels of SCLC-BVG marker genes, including collagen IV, αSMA, and ZO-1, which are indicative of basement membrane integrity, pericyte coverage, and tight junctions, respectively, in these pan-NE tumors, but not in non-NE tumors (Figure 7C).

We next explored whether the ASCL1-IGFBP5-IGF1R axis was associated with the presence of BVG structures and their role in immunosuppression in pan-NE tumor patients (Table S6). In a cohort of pan-NE tumor patients, *IGFBP5* expression was significantly upregulated in patients with high *ASCL1* expression compared to those with low *ASCL1* expression. Similar trends were observed in P-NEC, small intestine NEC (SI-NEC), and RE-NEC[59] cohorts and CRPC cohorts (Figures 7D–7F; Table S6).[59,60] Ranking pan-NE tumor patients by *ASCL1* expression levels revealed a progressive increase in *IGFBP5* expression, indicating a strong correlation between *IGFBP5* and *ASCL1* in pan-NE tumors (Figure 7G; Table S6). Further, we analyzed scRNA-seq data from 13 CRPC patients, including 3 CRPC-NE tumors and 10 CRPC adenocarcinomas.[3] *ASCL1*^{high} CRPC-NE tumors displayed significantly higher IGFBP5 expression compared to *ASCL1*^{low} tumors (Figure 7H). Importantly, endothelial cells from *ASCL1*^{high} tumors exhibited marked activation of the IGF1 signaling pathway, along with upregulation of basement membrane genes (e.g., *COL4A1*, *COL4A2*, *NID1*, *NID2*, *COL18A1*, and *LAMB1*), the basement membrane assembly and organization pathways (Figures 7I and S7B). Furthermore, the endothelial barrier establishment pathway demonstrated a strong negative correlation with T cell infiltration in pan-NE tumors (Figure 7J; Table S6).

In summary, these findings demonstrate that BVG structures are a common feature of pan-NE tumors. These structures are closely associated with the ASCL1-IGFBP5-IGF1R axis and contribute to immunosuppression.

DISCUSSION

The cancer immune microenvironment is shaped by multiple factors that influence responses to immunotherapy.[62] Among these, physical barriers play a critical role by impeding immune cell infiltration, thereby contributing to the immune-desert phenotype observed in certain tumors.[63] Well-characterized immune-excluding barriers include cancer-associated fibroblasts (CAFs), a collagen-rich ECM, and tight cell-cell junctions.[17,64] In brain tumors and brain metastases, the BTB represents a unique vascular barrier, structurally resembling the BBB, which is considered a major contributor to the immune-excluded phenotype in these tumors.[19,21] In contrast, peripheral tumors typically exhibit leaky vasculature with minimal basement membrane deposition and sparse pericyte coverage, facilitating immune cell trafficking.[16,19] In this study, we identified a previously unrecognized vascular structure in NE tumors, which we term BVG due to its ability to restrict immune cell infiltration. These BBB-like structures are defined by endothelial tight junctions, a thickened basement membrane, and high pericyte coverage. Our findings suggest that BVG structures may contribute significantly to the immunosuppressive TME and poor immunotherapy responses in SCLC and other NECs. Functional vessels need to

Figure 4. SCLC tumor cells induce the BVG via the ASCL1-IGFBP5-IGF1R axis

(A) Venn plot illustrating the overlap among genes with ASCL1 binding at promoter regions, genes downregulated upon *Ascl1* knockout, and genes positively correlated with the BVG signature (left). Scatter plot showing the ranked adjusted correlation scores of the 126 overlapping genes with the BVG signature score (right).

(B) IF analysis of IGFBP5 in patient (top) and mouse (bottom) NSCLC (left) and SCLC (right) tumor samples. Scale bars, 20 μm.

(C) Western blot of ASCL1 and IGFBP5 in SHP77 genetically edited with sgScr and sg*ASCL1*.

(D) Representative H&E staining of paraffin-embedded mouse SCLC tumors edited with sgScr and sg*Igfbp5*. Scale bars, 20 μm. Bar plots quantify the average thickness of the BM in tumor blood vessels. Mean ± SD ($n = 5$). $^{**}p < 0.01$. Mann-Whitney test.

(E) TEM images of mouse SCLC tumor (left) and genetically edited with sg*Igfbp5* (right). EC, endothelial; AJ, adherens junction; BM, basement membrane; and TJ, tight junction. Scale bars, 1 μm, magnified region, 250 nm.

(F) Consecutive sections of mouse SCLC tumors edited with sgScr and sg*Igfbp5* were analyzed by IF for the expression of IGFBP5, CD31, αSMA, collagen IV, and ZO-1, as described in STAR Methods. Scale bars, 50 μm.

(G) Representative CD31 staining and Evans Blue dye images of orthotopic mouse SCLC tumor edited with sgScr (left) and sg*Igfbp5* (right). Scale bars, 20 μm. Bar plots show the quantification of the permeability of the tumor blood vessels. Mean ± SD ($n = 3$). $^{**}p < 0.01$, $^{****}p < 0.0001$. *t* test.

(H) Representative IF staining images of T cells in OVA-expressing mouse SCLC tumors edited with sgScr or sg*Igfbp5* after OT-1 T cell transfer. Scale bars, 20 μm. Bar plot shows the quantification of infiltrating T cells from 6 sections. Mean ± SD. $^{*}p < 0.05$, $^{***}p < 0.001$. *t* test.

(I) RNA (left) and protein (right) levels of the BVG signature in ECs from sgScr versus sg*Igfbp5* SCLC tumors. Two-sided Wilcoxon rank-sum test.

(J) RNA (left) and protein (right) levels of the IGF1/IGF1R pathway gene signature in ECs from sgScr versus sg*Igfbp5* SCLC tumors. Two-sided Wilcoxon rank-sum test.

(K) mIHC analysis of CD31, IGF1R, and IGF1 in mouse SCLC tumors with sgScr and sg*Igfbp5*. Scale bars, 50 μm, magnified region, 20 μm.

(L) Experimental strategy of tumor cell transplantation with ECs following *Igf1r* disruption or control. First, ECs were infected with lentivirus expressing sgScr or sg*Igf1r* together with mCherry. Second, the infected ECs were mixed with SCLC tumor cells and transplanted subcutaneously into mice. Third, the mice were sacrificed for the following analyses.

(M) Representative H&E staining of paraffin-embedded mouse SCLC tumors after endothelial *Igf1r* disruption. Scale bars, 20 μm. Bar plots quantify the average thickness of the BM in tumor blood vessels. Mean ± SD ($n = 3$). $^{****}p < 0.0001$. *t* test.

(N) IF analysis of CD31, mCherry, and CD3 in mouse SCLC tumors containing ECs infected with sgScr or sg*Igf1r*. Scale bars, 20 μm (left). Bar plot shows the quantification of infiltrating T cells (right). Mean ± SEM ($n = 3$). $^{*}p < 0.05$, *t* test.

(O) *IGFBP5* mRNA levels, *IGFBP5* protein levels, IGF1/IGF1R signature expression scores, and phosphorylation levels of IGF1/IGF1R signature genes in *ASCL1*^{low} and *ASCL1*^{high} SCLC patients from the Liu et al.[9] TU cohort. $p < 0.05$. Two-sided Wilcoxon rank-sum test.

See also Figure S4.

Please cite this article in press as: Wang et al., A blood-brain barrier-like vascular gate limits immunotherapy efficacy in neuroendocrine cancers, Cell (2026), https://doi.org/10.1016/j.cell.2026.04.017

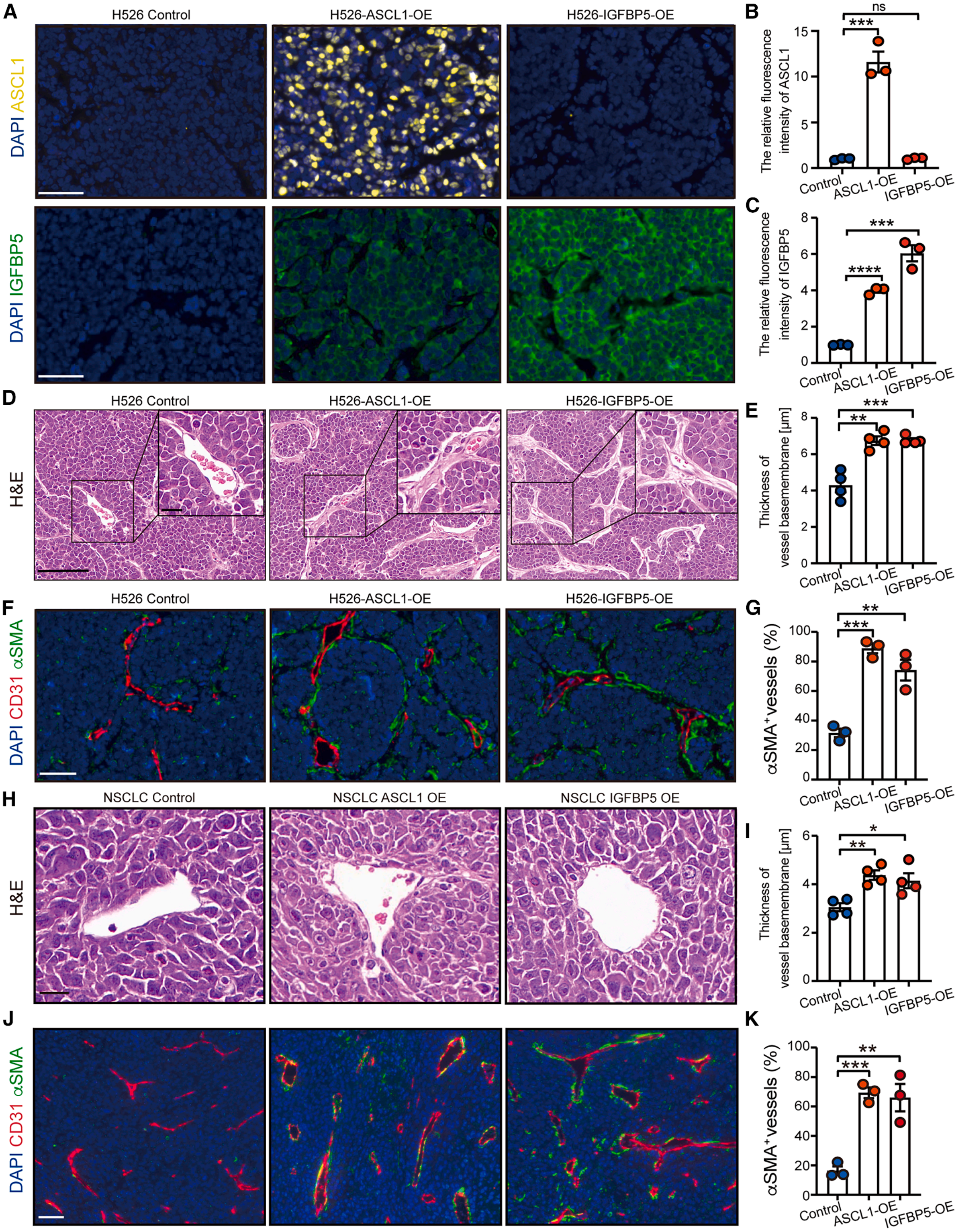

Figure 5. ASCL1 and IGFBP5 are sufficient to induce the BVG structure

(A–C) Representative IF staining of ASCL1 and IGFBP5 in paraffin-embedded H526 tumors overexpressing ASCL1 or IGFBP5. Scale bars, 50 μm (A). Relative ASCL1 (B) and IGFBP5 (C) fluorescence intensity in the indicated tumors. Mean ± SEM (*n* = 3). ns, not significant, $^{***}p < 0.001$; $^{****}p < 0.0001$, *t* test.

(D and E) Representative H&E staining of paraffin-embedded H526 tumors overexpressing ASCL1 or IGFBP5. Scale bars, 100 μm, magnified region, 20 μm (D). Bar plots quantify the average thickness of the BM in tumor blood vessels (E). Mean ± SEM (*n* = 4). $^{**}p < 0.01$; $^{***}p < 0.001$, *t* test.

(F and G) IF analysis of CD31 and αSMA in H526 tumors overexpressing ASCL1 or IGFBP5. Scale bars, 50 μm (F). Bar plots quantify the percentage of αSMA^+ vessels in tumor samples (G). Mean ± SEM (*n* = 3). $^{**}p < 0.01$; $^{***}p < 0.001$, *t* test.

(legend continued on next page)

Please cite this article in press as: Wang et al., A blood-brain barrier-like vascular gate limits immunotherapy efficacy in neuroendocrine cancers, Cell (2026), https://doi.org/10.1016/j.cell.2026.04.017

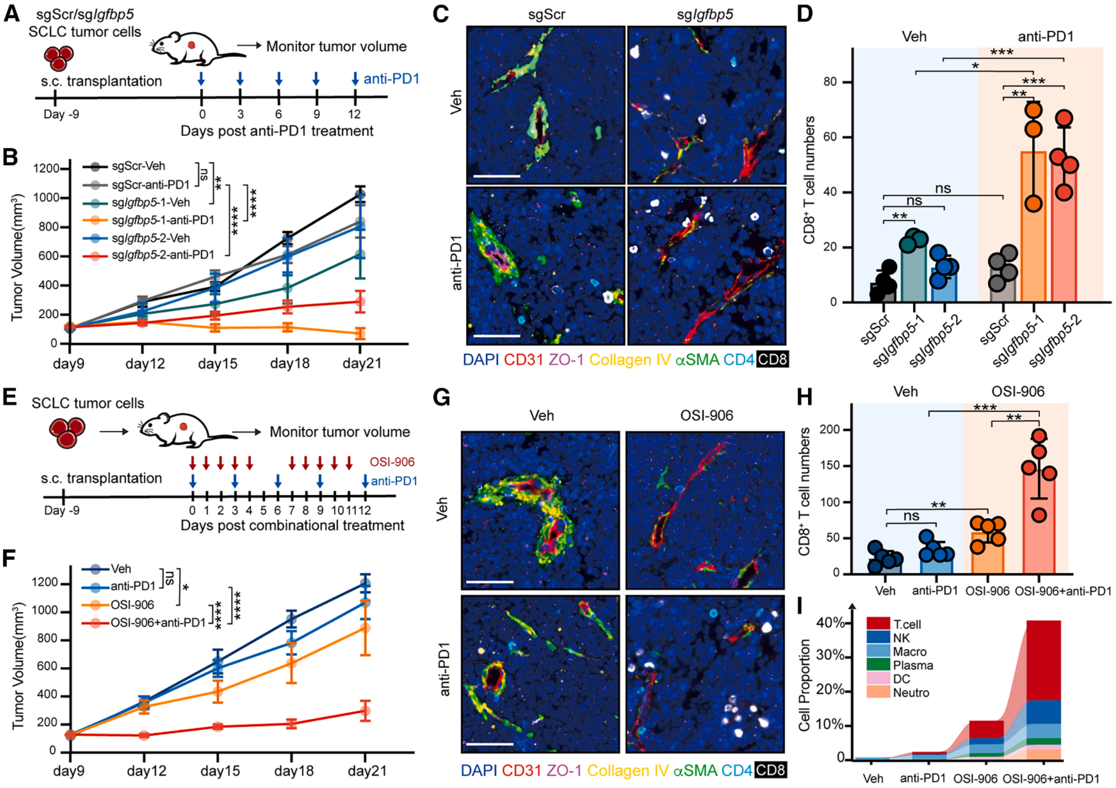

Figure 6. Targeting the ASCL1-IGFBP5-IGF1R axis improves immunotherapy efficacy in SCLC

(A) The experimental strategy for the ICI treatment of mouse SCLC tumor edited with sgScr and sg*Igfbp5* in C57BL/6.

(B) The subcutaneous tumor growth curve of immunotherapy in SCLC tumor edited with sgScr and sg*Igfbp5*. ns, not significant. Mean ± SEM (n = 4–5 biological replicates per group). $^{**}p < 0.01$. $^{****}p < 0.0001$. Two-way ANOVA.

(C and D) mIHC analysis of CD31, αSMA, ZO-1, collagen IV, CD4, and CD8 in mouse SCLC tumors with sgScr and sg*Igfbp5* treated with vehicle or anti-PD1. Scale bars, 50 μm (C). Bar plots show the quantification of infiltrating T cells (D). Mean ± SD (n = 3–4 biological replicates per group). ns, not significant, $^{**}p < 0.01$, $^{***}p < 0.001$, t test.

(E) Experimental strategy for ICI (anti-PD1) combined with IGF1R inhibitor (OSI-906) treatment in SCLC.

(F) The subcutaneous tumor growth curve of immunotherapy combined with IGF1R inhibitor in SCLC. ns, not significant. Mean ± SEM (n = 5–6 biological replicates per group). $^{*}p < 0.05$ and $^{****}p < 0.0001$. Two-way ANOVA.

(G and H) mIHC analysis of CD31, αSMA, ZO-1, collagen IV, CD4, and CD8 in SCLC tumors treated with vehicle, anti-PD1, OSI-906, and anti-PD1+ OSI-906. Scale bars, 50 μm (G). Bar plots show the quantification of infiltrating CD8^{+} T cells (H). Mean ± SD (n = 5 biological replicates per group). ns, not significant, $^{**}p < 0.01$, $^{***}p < 0.001$, t test.

(I) Immune cell infiltration levels in tumor tissues of SCLC mice treated with vehicle, anti-PD1, OSI-906, and anti-PD1 + OSI-906 in the single-cell transcriptomic data.

See also Figure S6.

balance the flow rate in the vessels and the exchange efficiency of their cargo with the tissues. It has been proposed that anti-vascular endothelial growth factor/vascular endothelial growth factor receptor (anti-VEGF/VEGFR) agents could "normalize" the leaky vessels to improve the delivery of other anti-tumor drugs with increased blood flow in various cancers, including NSCLC, colorectal cancer (CRC), renal cell carcinoma (RCC), and hepatocellular carcinoma (HCC).[65] Given the caveat of impermeability of BVG to immune cells in NECs, we propose to normalize them by increasing their leakiness to improve immunotherapy efficacy.

Our findings demonstrate that NE tumor cells play a pivotal role in the formation of these BVG structures via the ASCL1-IGFBP5-IGF1R axis. While the BTB in brain tumors is thought to originate from the normal BBB,[20] it remains unclear whether tumor cells contribute to its formation. Here, we showed that NE tumor cells are sufficient to generate BVG structures both orthotopically and ectopically. Specifically, NE tumor cells secrete

(H and I) Representative H&E staining of paraffin-embedded NSCLC tumors overexpressing ASCL1 or IGFBP5. Scale bars, 20 μm (H). Bar plots quantify the average thickness of the BM in tumor blood vessels (I). Mean ± SEM (n = 4). $^{*}p < 0.05$; $^{**}p < 0.01$, t test.

(J and K) IF analysis of CD31 and αSMA in NSCLC tumors overexpressing ASCL1 or IGFBP5. Scale bars, 50 μm (J). Bar plots quantify the percentage of αSMA^{+} vessels in tumor samples (K). Mean ± SEM (n = 3). $^{**}p < 0.01$; $^{***}p < 0.001$, t test.

See also Figure S5.

Please cite this article in press as: Wang et al., A blood-brain barrier-like vascular gate limits immunotherapy efficacy in neuroendocrine cancers, Cell (2026), https://doi.org/10.1016/j.cell.2026.04.017

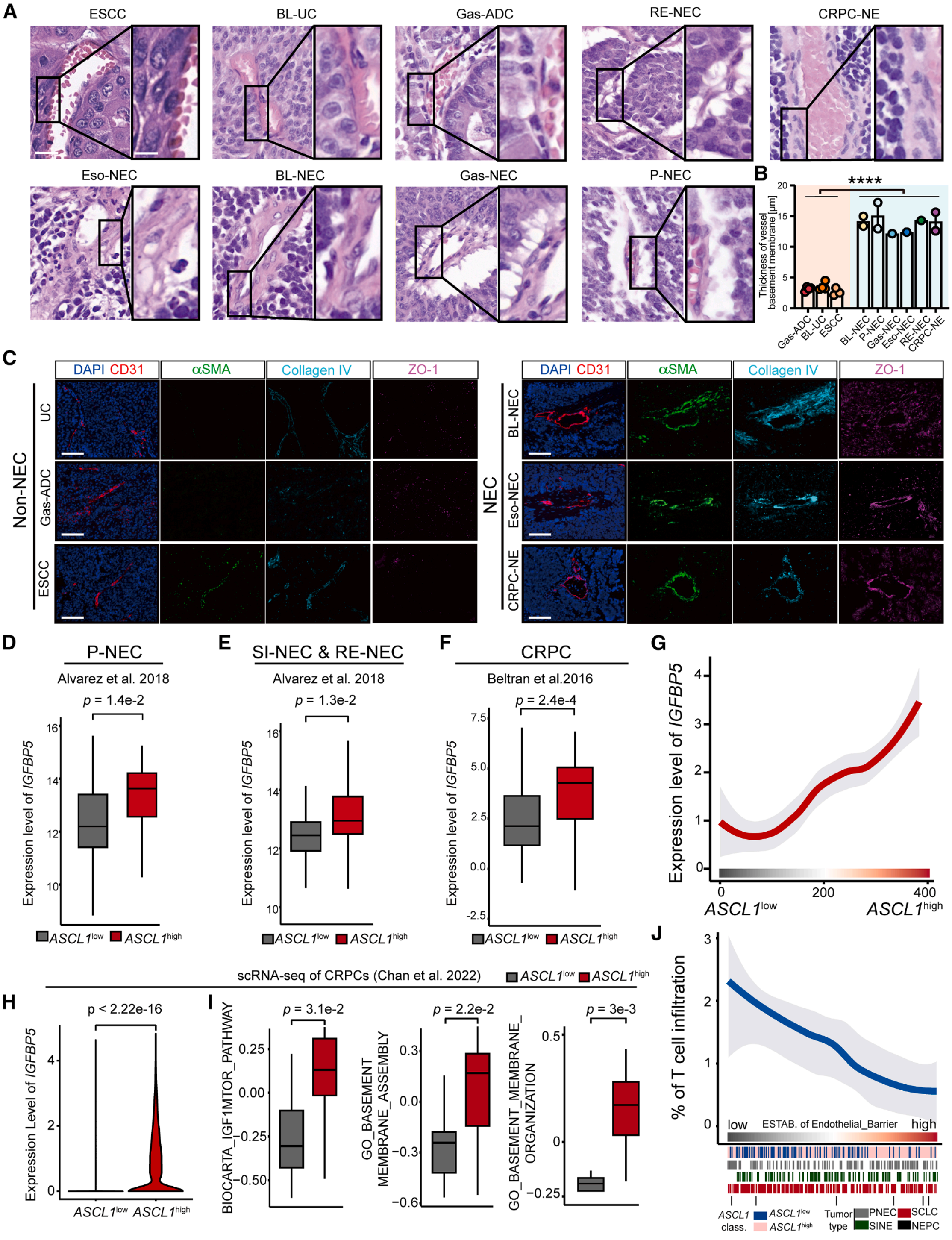

Figure 7. Pan-NE tumors exhibit a similar IEV barrier

(A and B) Representative H&E staining of paraffin-embedded patient tumor samples from with esophageal squamous cell carcinoma (ESCC), Eso-NEC, bladder urothelial carcinoma (BL-UC), BL-NEC, gastric adenocarcinoma (Gas-ADC), Gas-NEC, castration-resistant neuroendocrine prostate cancer (CRPC-NE), P-NEC, and rectal NEC (RE-NEC). Scale bars, 20 μm, magnified region, 10 μm (A). Quantification of the average thickness of the BM in tumor blood vessels (B). Data indicate mean ± SEM ($n_{\text{ESCC}} = 3$; $n_{\text{Eso-NEC}} = 1$; $n_{\text{BL-UC}} = 4$; $n_{\text{BL-NEC}} = 2$; $n_{\text{Gas-ADC}} = 4$; $n_{\text{Gas-NEC}} = 1$; $n_{\text{CRPC-NE}} = 2$; $n_{\text{P-NEC}} = 2$; $n_{\text{RE-NEC}} = 1$). ****$p < 0.0001$. Mann-Whitney test.

(C) Consecutive sections of patient non-NE and NE tumors were analyzed by IF for the expression of CD31, αSMA, collagen IV, and ZO-1, as described in STAR Methods. Scale bars, 100 μm.

(legend continued on next page)

IGFBP5, a direct downstream target of ASCL1, the master transcription factor in NE tumors. IGFBP5 may facilitate IGF1 delivery and activate the IGF1/IGF1R signaling pathway in endothelial cells. It would be of interest to investigate whether the ASCL1-IGFBP5-IGF1R axis also plays a role in BTB and even BBB formation.

The discovery of BVG structures and their underlying molecular mechanisms in NE tumors opens avenues for novel therapeutic strategies. As these structures are less permeable and contribute to the immunosuppressive microenvironment, targeting them could enhance immune cell infiltration and improve patient outcomes. We demonstrated that both genetic and pharmacological inhibition of IGFBP5 and IGF1R disrupted BVG structures, increased CD8$^+$ T cell infiltration, and significantly enhanced the efficacy of immunotherapy in SCLC. Notably, the IGF1R inhibitor OSI-906 has been shown to be clinically safe. Although it has limited clinical efficacy as a monotherapy,[58,66] our findings suggest that combining OSI-906 with immunotherapy could be a promising treatment strategy for SCLC and other NE tumors.

Limitations of the study

This study identifies a BVG structure in SCLC and suggests that it may physically prevent immune cell infiltration. Whether the altered features of endothelial cells and associated components, such as pericytes and the basement membrane, contribute to immune resistance and malignancy in SCLC beyond their role as a physical barrier remains to be investigated. Furthermore, we observed similar BVG structures in other NECs based on histological and gene expression analyses; however, functional validation of these BVGs in other NECs is still lacking.

Given the ASCL1-IGFBP5-IGF1R axis underlying the BVG, we propose that targeting IGF1R could convert SCLC from a “cold” to a “hot” tumor, thereby synergizing with immunotherapy. Considering the structural similarity between the BVG and the BBB, it is important to evaluate the potential effects of IGF1R inhibitors on the BBB. Additionally, further investigation is needed to assess the efficacy and side effects of IGF1R inhibition alone and in combination with immunotherapy in patients.

RESOURCE AVAILABILITY

Lead contact

Requests for further information and resources should be directed to and will be fulfilled by the lead contact, Chong Chen (chongchen@scu.edu.cn).

Materials availability

All unique reagents generated in this study are available from the lead contact with a completed materials transfer agreement.

Data and code availability

- The raw and processed bulk RNA-seq and single-cell RNA-seq data generated in this study have been deposited in GEO: GSE287964 (https://www.ncbi.nlm.nih.gov/geo/query/acc.cgi?acc=GSE287964) and are publicly available. The proteomics data generated in this study have been deposited in OMIX: OMIX016097 and are publicly available. Previously published multi-omics datasets reanalyzed in this study are listed in the key resources table under “Deposited data,” together with their original publications and accession numbers.
- The analysis codes can be found on GitHub (https://github.com/AilingZhong/SCLC_ICI_Project).
- Any additional information required to reanalyze the data reported in this paper is available from the lead contact upon request.

ACKNOWLEDGMENTS

We gratefully acknowledge Dr. Yuquan Wei and Dr. Xiuwu Bian for their generous support and all of the CC-LY laboratory members for their insightful advice and kind assistance. We thank the Core Facilities of West China Hospital, Chengdu OrganoidMed Medical Laboratory, and Chengdu LUMINIRIS Bio Tech Co., Ltd. for their technical support. The work was supported by the National Natural Science Foundation of China (82330087, U25C2036, 32595480, T2221004, 82130007, 82170171, 82470188, 82503629, 82300186, 82303880, and 82472783); Noncommunicable Chronic Diseases-National Science and Technology Major Project (2023ZD0500500); the National Key Research and Development Program of China (2024YFF0507402); Health Commission of Sichuan Province (24CXTD05); the Sichuan Science and Technology Program (2025ZNSFSC0273, 2025ZYD0164, 2025NSFTD0030, 2025ZNSFSC0047, 2023NSFSC1904, and 2024NSFSC1699); the Key R&D Projects of the Health Commission of Sichuan Province, China (24LCYJZD09); the Regional Innovation Cooperation Project of the Science and Technology Department of Sichuan Province (2026YFHZ0148); the Frontiers Medical Center, Tianfu Jincheng Laboratory Foundation (TFJC2023010004); the National Clinical Research Center for Geriatrics, West China Hospital, Sichuan University (Z2024JC001); the Science and Technology Bureau of Chengdu (2026-YF09-00036-SN); the China Postdoctoral Science Foundation (2023M732457); Project for Enhancing Young Teachers' Scientific and Technological Innovation Ability of Sichuan University (2024SCUQJTX042); and Post-Doctor Research Project, West China Hospital, Sichuan University (2024HXBH179). The schematics were created using BioRender.

AUTHOR CONTRIBUTIONS

Conceptualization, Y.L., Yiyun Wang, and C.C.; methodology, Yiyun Wang, A.Z., Bo Wang, Jian Zhong, Zuoyu Liang, Zhiming Li, M.W., Y.L., and C.C.; investigation, Yiyun Wang, A.Z., Bo Wang, X.Z., C.L., X.D., C.X., Jianan Zheng, Baohong Wu, L.Z., Yuying Wang, and X.L.; resources, X.Z., J.W., M.Z., H.L., X.W., S.D., Y.Y., S.Z., W.W., S.Y., J.X., C.Z., Y.Z., M.W., Y.L., and C.C.; funding acquisition, Baohong Wu, S.Y., Y.Z., F.N., M.W., Y.L., and C.C.;

(D–F) *IGFBP5* expression levels in *ASCL1*^{low} and *ASCL1*^{high} pan-NECs. P-NEC, pancreatic neuroendocrine cancer (n = 97 *ASCL1*^{low}, n = 16 *ASCL1*^{high}) (D); SI-NEC and RE-NEC, small intestinal and rectal NECs (n = 29 *ASCL1*^{low}, n = 70 *ASCL1*^{high}) (E) from Alvarez et al.[59]; CRPC, castration-resistant prostate cancer from Beltran et al.[60] (n = 19 *ASCL1*^{low}, n = 30 *ASCL1*^{high}) (F). Two-sided Wilcoxon rank-sum test.

(G) *IGFBP5* expression across pan-ne tumor samples ranked by *ASCL1* expression: P-NEC (n = 113), SI-NEC and RE-NEC (n = 99), SCLC from George et al.[45] (n = 113), SCLC from Liu et al.[9] (n = 81), and CRPC-NE from Abida et al.[61] (n = 6).

(H) *IGFBP5* expression levels in *ASCL1*^{low} and *ASCL1*^{high} tumor cells from CRPC patients, based on scRNA-seq data from Chan et al.[3] (CRPC-Adeno, n = 10 patients; CRPC-NE, n = 3 patients).

(I) GSVA scores of IGF1 and BM-associated pathways in ECs from CRPC-Adeno and CRPC-NE patients. Unpaired two-tailed t test.

(J) GSVA scores for endothelial barrier establishment according to T cell infiltration in pan-NEC cohorts: P-NEC (n = 113), SI-NEC, and RE-NEC (n=99) from Alvarez et al.,[59] and SCLC from George et al.[45] (n = 113) and Liu et al.[9] (n = 81).

See also Figure S7.

supervision, F.N., M.W., Y.L., and C.C.; writing—original draft, Yiyun Wang, A.Z., Bo Wang, Y.L., and C.C.; and writing—review and editing, Yiyun Wang, A.Z., Bo Wang, X.Z., T.T., M.W., Y.L., and C.C.

DECLARATION OF INTERESTS

The authors declare no competing interests.

STAR★METHODS

Detailed methods are provided in the online version of this paper and include the following:

- KEY RESOURCES TABLE
- METHOD DETAILS
  - Mice
  - Human specimens
  - Cell line
  - Organoid culture
  - Isolation and Sorting of Endothelial Cells (ECs) from Tumor/Normal Tissues
  - Gene editing
  - Mouse models generation
  - *In vivo* treatment
  - OT-1 T cell culture
  - RNA extraction and quantitative PCR
  - Intratumoral pH measurement
  - Doppler ultrasound imaging
  - Tumor vascular perfusion assay
  - Spatial proteomics mass spectrometry approach
  - Transmission electron microscope
  - Determination of vascular permeability
  - H&E, immunohistochemistry, and immunofluorescence staining
  - Analysis of the basement membrane thickness of tumor blood vessels
  - Computational methods
  - Clinical and public cohort analyses
- QUANTIFICATION AND STATISTICAL ANALYSIS

SUPPLEMENTAL INFORMATION

Supplemental information can be found online at https://doi.org/10.1016/j.cell.2026.04.017.

Received: May 28, 2025
Revised: January 5, 2026
Accepted: April 9, 2026

REFERENCES

1. Sen, T., Dotsu, Y., Corbett, V., Puri, S., Sen, U., Boyle, T.A., Mack, P., Hirsch, F., Aljumaily, R., Naqash, A.R., et al. (2025). Pulmonary neuroendocrine neoplasms: the molecular landscape, therapeutic challenges, and diagnosis and management strategies. Lancet Oncol. *26*, e13–e33. https://doi.org/10.1016/S1470-2045(24)00374-7.
2. Auernhammer, C.J., Spitzweg, C., Angele, M.K., Boeck, S., Grossman, A., Nölting, S., Ilhan, H., Knösel, T., Mayerle, J., Reincke, M., et al. (2018). Advanced neuroendocrine tumours of the small intestine and pancreas: clinical developments, controversies, and future strategies. Lancet Diabetes Endocrinol. *6*, 404–415. https://doi.org/10.1016/S2213-8587(17)30401-1.
3. Chan, J.M., Zaidi, S., Love, J.R., Zhao, J.L., Setty, M., Wadosky, K.M., Gopalan, A., Choo, Z.N., Persad, S., Choi, J., et al. (2022). Lineage plasticity in prostate cancer depends on JAK/STAT inflammatory signaling. Science *377*, 1180–1191. https://doi.org/10.1126/science.abn0478.
4. Chen, C.C., Tran, W., Song, K., Sugimoto, T., Obusan, M.B., Wang, L., Sheu, K.M., Cheng, D., Ta, L., Varuzhanyan, G., et al. (2023). Temporal evolution reveals bifurcated lineages in aggressive neuroendocrine small cell prostate cancer trans-differentiation. Cancer Cell *41*, 2066–2082.e9. https://doi.org/10.1016/j.ccell.2023.10.009.
5. Feng, M., Matoso, A., Epstein, G., Fong, M., Park, Y.H., Gabrielson, A., Patel, S., Czerniak, B., Compérat, E., Hoffman-Censits, J., et al. (2024). Identification of Lineage-specific Transcriptional Factor-defined Molecular Subtypes in Small Cell Bladder Cancer. Eur. Urol. *85*, 523–526. https://doi.org/10.1016/j.eururo.2023.05.023.
6. Chan, J.M., Quintanal-Villalonga, Á., Gao, V.R., Xie, Y., Allaj, V., Chaudhary, O., Masilionis, I., Egger, J., Chow, A., Walle, T., et al. (2021). Signatures of plasticity, metastasis, and immunosuppression in an atlas of human small cell lung cancer. Cancer Cell *39*, 1479–1496.e18. https://doi.org/10.1016/j.ccell.2021.09.008.
7. Wang, Z., Liu, C., Zheng, S., Yao, Y., Wang, S., Wang, X., Yin, E., Zeng, Q., Zhang, C., Zhang, G., et al. (2024). Molecular subtypes of neuroendocrine carcinomas: A cross-tissue classification framework based on five transcriptional regulators. Cancer Cell *42*, 1106–1125.e8. https://doi.org/10.1016/j.ccell.2024.05.002.
8. Gay, C.M., Stewart, C.A., Park, E.M., Diao, L., Groves, S.M., Heeke, S., Nabet, B.Y., Fujimoto, J., Solis, L.M., Lu, W., et al. (2021). Patterns of transcription factor programs and immune pathway activation define four major subtypes of SCLC with distinct therapeutic vulnerabilities. Cancer Cell *39*, 346–360.e7. https://doi.org/10.1016/j.ccell.2020.12.014.
9. Liu, Q., Zhang, J., Guo, C., Wang, M., Wang, C., Yan, Y., Sun, L., Wang, D., Zhang, L., Yu, H., et al. (2024). Proteogenomic characterization of small cell lung cancer identifies biological insights and subtype-specific therapeutic strategies. Cell *187*, 184–203.e28. https://doi.org/10.1016/j.cell.2023.12.004.
10. Takkenkamp, T.J., Jalving, M., Hoogwater, F.J.H., and Walenkamp, A.M.E. (2020). The immune tumour microenvironment of neuroendocrine tumours and its implications for immune checkpoint inhibitors. Endocr. Relat. Cancer *27*, R329–R343. https://doi.org/10.1530/ERC-20-0113.
11. Horn, L., Mansfield, A.S., Szczęsna, A., Havel, L., Krzakowski, M., Hochmair, M.J., Huemer, F., Losonczy, G., Johnson, M.L., Nishio, M., et al. (2018). First-Line Atezolizumab plus Chemotherapy in Extensive-Stage Small-Cell Lung Cancer. N. Engl. J. Med. *379*, 2220–2229. https://doi.org/10.1056/NEJMoa1809064.
12. Paz-Ares, L., Dvorkin, M., Chen, Y., Reinmuth, N., Hotta, K., Trukhin, D., Statsenko, G., Hochmair, M.J., Özgüroğlu, M., Ji, J.H., et al. (2019). Durvalumab plus platinum-etoposide versus platinum-etoposide in first-line treatment of extensive-stage small-cell lung cancer (CASPIAN): a randomised, controlled, open-label, phase 3 trial. Lancet *394*, 1929–1939. https://doi.org/10.1016/S0140-6736(19)32222-6.
13. Martínez-Jiménez, F., Movasati, A., Brunner, S.R., Nguyen, L., Priestley, P., Cuppen, E., and Van Hoeck, A. (2023). Pan-cancer whole-genome comparison of primary and metastatic solid tumours. Nature *618*, 333–341. https://doi.org/10.1038/s41586-023-06054-z.
14. Alexandrov, L.B., Nik-Zainal, S., Wedge, D.C., Aparicio, S.A.J.R., Behjati, S., Biankin, A.V., Bignell, G.R., Bolli, N., Borg, A., Børresen-Dale, A.L., et al. (2013). Signatures of mutational processes in human cancer. Nature *500*, 415–421. https://doi.org/10.1038/nature12477.
15. Jain, R.K. (2014). Antiangiogenesis strategies revisited: from starving tumors to alleviating hypoxia. Cancer Cell *26*, 605–622. https://doi.org/10.1016/j.ccell.2014.10.006.
16. Carmeliet, P., and Jain, R.K. (2011). Principles and mechanisms of vessel normalization for cancer and other angiogenic diseases. Nat. Rev. Drug Discov. *10*, 417–427. https://doi.org/10.1038/nrd3455.
17. Augustin, H.G., and Koh, G.Y. (2024). A systems view of the vascular endothelium in health and disease. Cell *187*, 4833–4858. https://doi.org/10.1016/j.cell.2024.07.012.
18. Wang, C., Zeng, Q., Gül, Z.M., Wang, S., Pick, R., Cheng, P., Bill, R., Wu, Y., Naulaerts, S., Barnoud, C., et al. (2024). Circadian tumor infiltration and

function of CD8+ T cells dictate immunotherapy efficacy. Cell *187*, 2690–2702.e17. https://doi.org/10.1016/j.cell.2024.04.015.

19. Steeg, P.S. (2021). The blood-tumour barrier in cancer biology and therapy. Nat. Rev. Clin. Oncol. *18*, 696–714. https://doi.org/10.1038/s41571-021-00529-6.
20. Arvanitis, C.D., Ferraro, G.B., and Jain, R.K. (2020). The blood-brain barrier and blood-tumour barrier in brain tumours and metastases. Nat. Rev. Cancer *20*, 26–41. https://doi.org/10.1038/s41568-019-0205-x.
21. Zhao, Z., Nelson, A.R., Betsholtz, C., and Zlokovic, B.V. (2015). Establishment and Dysfunction of the Blood-Brain Barrier. Cell *163*, 1064–1078. https://doi.org/10.1016/j.cell.2015.10.067.
22. Ravi, A., Hellmann, M.D., Arniella, M.B., Holton, M., Freeman, S.S., Naranbhai, V., Stewart, C., Leshchiner, I., Kim, J., Akiyama, Y., et al. (2023). Genomic and transcriptomic analysis of checkpoint blockade response in advanced non-small cell lung cancer. Nat. Genet. *55*, 807–819. https://doi.org/10.1038/s41588-023-01355-5.
23. Rose, T.L., Weir, W.H., Mayhew, G.M., Shibata, Y., Eulitt, P., Uronis, J.M., Zhou, M., Nielsen, M., Smith, A.B., Woods, M., et al. (2021). Fibroblast growth factor receptor 3 alterations and response to immune checkpoint inhibition in metastatic urothelial cancer: a real world experience. Br. J. Cancer *125*, 1251–1260. https://doi.org/10.1038/s41416-021-01488-6.
24. Robertson, A.G., Meghani, K., Cooley, L.F., McLaughlin, K.A., Fall, L.A., Yu, Y., Castro, M.A.A., Groeneveld, C.S., de Reyniès, A., Nazarov, V.I., et al. (2023). Expression-based subtypes define pathologic response to neoadjuvant immune-checkpoint inhibitors in muscle-invasive bladder cancer. Nat. Commun. *14*, 2126. https://doi.org/10.1038/s41467-023-37568-9.
25. Zhao, J., Chen, A.X., Gartrell, R.D., Silverman, A.M., Aparicio, L., Chu, T., Bordbar, D., Shan, D., Samanamud, J., Mahajan, A., et al. (2019). Immune and genomic correlates of response to anti-PD-1 immunotherapy in glioblastoma. Nat. Med. *25*, 462–469. https://doi.org/10.1038/s41591-019-0349-y.
26. Hugo, W., Zaretsky, J.M., Sun, L., Song, C., Moreno, B.H., Hu-Lieskovan, S., Berent-Maoz, B., Pang, J., Chmielowski, B., Cherry, G., et al. (2016). Genomic and Transcriptomic Features of Response to Anti-PD-1 Therapy in Metastatic Melanoma. Cell *165*, 35–44. https://doi.org/10.1016/j.cell.2016.02.065.
27. Riaz, N., Havel, J.J., Makarov, V., Desrichard, A., Urba, W.J., Sims, J.S., Hodi, F.S., Martín-Algarra, S., Mandal, R., Sharfman, W.H., et al. (2017). Tumor and Microenvironment Evolution during Immunotherapy with Nivolumab. Cell *171*, 934–949.e16. https://doi.org/10.1016/j.cell.2017.09.028.
28. Lauss, M., Donia, M., Harbst, K., Andersen, R., Mitra, S., Rosengren, F., Salim, M., Vallon-Christersson, J., Törngren, T., Kvist, A., et al. (2017). Mutational and putative neoantigen load predict clinical benefit of adoptive T cell therapy in melanoma. Nat. Commun. *8*, 1738. https://doi.org/10.1038/s41467-017-01460-0.
29. Liu, D., Schilling, B., Liu, D., Sucker, A., Livingstone, E., Jerby-Arnon, L., Zimmer, L., Gutzmer, R., Satzger, I., Loquai, C., et al. (2019). Integrative molecular and clinical modeling of clinical outcomes to PD1 blockade in patients with metastatic melanoma. Nat. Med. *25*, 1916–1927. https://doi.org/10.1038/s41591-019-0654-5.
30. Limagne, E., Nuttin, L., Thibaudin, M., Jacquin, E., Aucagne, R., Bon, M., Revy, S., Barnestein, R., Ballot, E., Truntzer, C., et al. (2022). MEK inhibition overcomes chemoimmunotherapy resistance by inducing CXCL10 in cancer cells. Cancer Cell *40*, 136–152.e12. https://doi.org/10.1016/j.ccell.2021.12.009.
31. Reinstein, Z.Z., Zhang, Y., Ospina, O.E., Nichols, M.D., Chu, V.A., Pulido, A.M., Prieto, K., Nguyen, J.V., Yin, R., Moran Segura, C., et al. (2024). Preexisting skin-resident CD8 and γδ T-cell circuits mediate immune response in Merkel cell carcinoma and predict immunotherapy efficacy. Cancer Discov. *14*, 1631–1652. https://doi.org/10.1158/2159-8290.CD-23-0798.
32. George, J., Maas, L., Abedpour, N., Cartolano, M., Kaiser, L., Fischer, R.N., Scheel, A.H., Weber, J.P., Hellmich, M., Bosco, G., et al. (2024). Evolutionary trajectories of small cell lung cancer under therapy. Nature *627*, 880–889. https://doi.org/10.1038/s41586-024-07177-7.
33. Nabet, B.Y., Hamidi, H., Lee, M.C., Banchereau, R., Morris, S., Adler, L., Gayevskiy, V., Elhossiny, A.M., Srivastava, M.K., Patil, N.S., et al. (2024). Immune heterogeneity in small-cell lung cancer and vulnerability to immune checkpoint blockade. Cancer Cell *42*, 429–443.e4. https://doi.org/10.1016/j.ccell.2024.01.010.
34. Na, F., Pan, X., Chen, J., Chen, X., Wang, M., Chi, P., You, L., Zhang, L., Zhong, A., Zhao, L., et al. (2022). KMT2C deficiency promotes small cell lung cancer metastasis through DNMT3A-mediated epigenetic reprogramming. Nat. Cancer *3*, 753–767. https://doi.org/10.1038/s43018-022-00361-6.
35. Meuwissen, R., Linn, S.C., Linnoila, R.I., Zevenhoven, J., Mooi, W.J., and Berns, A. (2003). Induction of small cell lung cancer by somatic inactivation of both Trp53 and Rb1 in a conditional mouse model. Cancer Cell *4*, 181–189. https://doi.org/10.1016/S1535-6108(03)00220-4.
36. Mollaoglu, G., Guthrie, M.R., Böhm, S., Brägelmann, J., Can, I., Ballieu, P.M., Marx, A., George, J., Heinen, C., Chalishazar, M.D., et al. (2017). MYC Drives Progression of Small Cell Lung Cancer to a Variant Neuroendocrine Subtype with Vulnerability to Aurora Kinase Inhibition. Cancer Cell *31*, 270–285. https://doi.org/10.1016/j.ccell.2016.12.005.
37. Wang, M., Wang, Y., Pan, X., Wang, B., Wang, Y., Luo, X., Deng, X., Liu, L., Chen, X., Zhai, X., et al. (2025). Acquired resistance to immunotherapy by physical barriers with cancer cell-expressing collagens in non-small cell lung cancer. Proc. Natl. Acad. Sci. USA *122*, e2500019122. https://doi.org/10.1073/pnas.2500019122.
38. Wang, J., Du, J., Luo, X., Guo, L., Liu, Y., Zhou, J., Zou, Y., Lu, Z., Pan, X., Chen, X., et al. (2024). A platform of functional studies of ESCC-associated gene mutations identifies the roles of TGFBR2 in ESCC progression and metastasis. Cell Rep. *43*, 114952. https://doi.org/10.1016/j.celrep.2024.114952.
39. Chen, J., Zhao, L., Peng, H., Dai, S., Quan, Y., Wang, M., Wang, J., Bi, Z., Zheng, Y., Zhou, S., et al. (2021). An organoid-based drug screening identified a menin-MLL inhibitor for endometrial cancer through regulating the HIF pathway. Cancer Gene Ther. *28*, 112–125. https://doi.org/10.1038/s41417-020-0190-y.
40. Lu, Z., Zhong, A., Liu, H., Zhang, M., Chen, X., Pan, X., Wang, M., Deng, X., Gao, L., Zhao, L., et al. (2022). Dissecting the genetic and microenvironmental factors of gastric tumorigenesis in mice. Cell Rep. *41*, 111482. https://doi.org/10.1016/j.celrep.2022.111482.
41. Wang, M., Chen, X., Tan, P., Wang, Y., Pan, X., Lin, T., Jiang, Y., Wang, B., Xu, H., Wang, Y., et al. (2022). Acquired semi-squamatization during chemotherapy suggests differentiation as a therapeutic strategy for bladder cancer. Cancer Cell *40*, 1044–1059.e8. https://doi.org/10.1016/j.ccell.2022.08.010.
42. Wang-Bishop, L., Kimmel, B.R., Ngwa, V.M., Madden, M.Z., Baljon, J.J., Florian, D.C., Hanna, A., Pastora, L.E., Sheehy, T.L., Kwiatkowski, A.J., et al. (2023). STING-activating nanoparticles normalize the vascular-immune interface to potentiate cancer immunotherapy. Sci. Immunol. *8*, eadd1153. https://doi.org/10.1126/sciimmunol.add1153.
43. Sun, Y., Chen, W., Torphy, R.J., Yao, S., Zhu, G., Lin, R., Lugano, R., Miller, E.N., Fujiwara, Y., Bian, L., et al. (2021). Blockade of the CD93 pathway normalizes tumor vasculature to facilitate drug delivery and immunotherapy. Sci. Transl. Med. *13*, eabc8922. https://doi.org/10.1126/scitranslmed.abc8922.
44. Zhao, J., Hu, S., Qi, Z., Xu, X., Long, X., Huang, A., Liu, J., and Cheng, P. (2024). Mitochondrial metabolic reprogramming of macrophages and T cells enhances CD47 antibody-engineered oncolytic virus antitumor immunity. J. Immunother. Cancer *12*, e009768. https://doi.org/10.1136/jitc-2024-009768.
45. George, J., Lim, J.S., Jang, S.J., Cun, Y., Ozretić, L., Kong, G., Leenders, F., Lu, X., Fernández-Cuesta, L., Bosco, G., et al. (2015). Comprehensive genomic profiles of small cell lung cancer. Nature *524*, 47–53. https://doi.org/10.1038/nature14664.

46. Redin, E., Sridhar, H., Zhan, Y.A., Pereira Mello, B., Zhong, H., Durani, V., Sabet, A., Manoj, P., Linkov, I., Qiu, J., et al. (2024). SMARCA4 controls state plasticity in small cell lung cancer through regulation of neuroendocrine transcription factors and REST splicing. J. Hematol. Oncol. *17*, 58. https://doi.org/10.1186/s13045-024-01572-3.

47. Borromeo, M.D., Savage, T.K., Kollipara, R.K., He, M., Augustyn, A., Osborne, J.K., Girard, L., Minna, J.D., Gazdar, A.F., Cobb, M.H., et al. (2016). ASCL1 and NEUROD1 Reveal Heterogeneity in Pulmonary Neuroendocrine Tumors and Regulate Distinct Genetic Programs. Cell Rep. *16*, 1259–1272. https://doi.org/10.1016/j.celrep.2016.06.081.

48. Rudin, C.M., Brambilla, E., Faivre-Finn, C., and Sage, J. (2021). Small-cell lung cancer. Nat. Rev. Dis. Primers *7*, 3. https://doi.org/10.1038/s41572-020-00235-0.

49. Olsen, R.R., Ireland, A.S., Kastner, D.W., Groves, S.M., Spainhower, K.B., Pozo, K., Kelenis, D.P., Whitney, C.P., Guthrie, M.R., Wait, S.J., et al. (2021). ASCL1 represses a SOX9(+) neural crest stem-like state in small cell lung cancer. Genes Dev. *35*, 847–869. https://doi.org/10.1101/gad.348295.121.

50. Wang, X.D., Hu, R., Ding, Q., Savage, T.K., Huffman, K.E., Williams, N., Cobb, M.H., Minna, J.D., Johnson, J.E., and Yu, Y. (2019). Subtype-specific secretomic characterization of pulmonary neuroendocrine tumor cells. Nat. Commun. *10*, 3201. https://doi.org/10.1038/s41467-019-11153-5.

51. Baxter, R.C. (2024). Endocrine and cellular physiology and pathology of the insulin-like growth factor acid-labile subunit. Nat. Rev. Endocrinol. *20*, 414–425. https://doi.org/10.1038/s41574-024-00970-4.

52. Baxter, R.C. (2014). IGF binding proteins in cancer: mechanistic and clinical insights. Nat. Rev. Cancer *14*, 329–341. https://doi.org/10.1038/nrc3720.

53. Langer, C.J., Novello, S., Park, K., Krzakowski, M., Karp, D.D., Mok, T., Benner, R.J., Scranton, J.R., Olszanski, A.J., and Jassem, J. (2014). Randomized, phase III trial of first-line figitumumab in combination with paclitaxel and carboplatin versus paclitaxel and carboplatin alone in patients with advanced non-small-cell lung cancer. J. Clin. Oncol. *32*, 2059–2066. https://doi.org/10.1200/JCO.2013.54.4932.

54. Libutti, S.K. (2013). Therapy: Blockade of IGF-1R-not effective in neuroendocrine tumours. Nat. Rev. Endocrinol. *9*, 389–390. https://doi.org/10.1038/nrendo.2013.109.

55. Macaulay, V.M., Middleton, M.R., Protheroe, A.S., Tolcher, A., Dieras, V., Sessa, C., Bahleda, R., Blay, J.Y., LoRusso, P., Mery-Mignard, D., et al. (2013). Phase I study of humanized monoclonal antibody AVE1642 directed against the type 1 insulin-like growth factor receptor (IGF-1R), administered in combination with anticancer therapies to patients with advanced solid tumors. Ann. Oncol. *24*, 784–791. https://doi.org/10.1093/annonc/mds511.

56. Schmitz, S., Kaminsky-Forrett, M.C., Henry, S., Zanetta, S., Geoffrois, L., Bompas, E., Moxhon, A., Mignion, L., Guigay, J., Knoops, L., et al. (2012). Phase II study of figitumumab in patients with recurrent and/or metastatic squamous cell carcinoma of the head and neck: clinical activity and molecular response (GORTEC 2008–02). Ann. Oncol. *23*, 2153–2161. https://doi.org/10.1093/annonc/mdr574.

57. Robertson, J.F., Ferrero, J.M., Bourgeois, H., Kennecke, H., de Boer, R.H., Jacot, W., McGreivy, J., Suzuki, S., Zhu, M., McCaffery, I., et al. (2013). Ganitumab with either exemestane or fulvestrant for postmenopausal women with advanced, hormone-receptor-positive breast cancer: a randomised, controlled, double-blind, phase 2 trial. Lancet Oncol. *14*, 228–235. https://doi.org/10.1016/S1470-2045(13)70026-3.

58. Chiappori, A.A., Otterson, G.A., Dowlati, A., Traynor, A.M., Horn, L., Owonikoko, T.K., Ross, H.J., Hann, C.L., Abu Hejleh, T., Nieva, J., et al. (2016). A Randomized Phase II Study of Linsitinib (OSI-906) Versus Topotecan in Patients With Relapsed Small-Cell Lung Cancer. Oncologist *21*, 1163–1164. https://doi.org/10.1634/theoncologist.2016-0220.

59. Alvarez, M.J., Subramaniam, P.S., Tang, L.H., Grunn, A., Aburi, M., Rieckhof, G., Komissarova, E.V., Hagan, E.A., Bodei, L., Clemons, P.A., et al. (2018). A precision oncology approach to the pharmacological targeting of mechanistic dependencies in neuroendocrine tumors. Nat. Genet. *50*, 979–989. https://doi.org/10.1038/s41588-018-0138-4.

60. Beltran, H., Prandi, D., Mosquera, J.M., Benelli, M., Puca, L., Cyrta, J., Marotz, C., Giannopoulou, E., Chakravarthi, B.V.S.K., Varambally, S., et al. (2016). Divergent clonal evolution of castration-resistant neuroendocrine prostate cancer. Nat. Med. *22*, 298–305. https://doi.org/10.1038/nm.4045.

61. Abida, W., Cyrta, J., Heller, G., Prandi, D., Armenia, J., Coleman, I., Cieslik, M., Benelli, M., Robinson, D., Van Allen, E.M., et al. (2019). Genomic correlates of clinical outcome in advanced prostate cancer. Proc. Natl. Acad. Sci. USA *116*, 11428–11436. https://doi.org/10.1073/pnas.1902651116.

62. Yan, C., Zheng, L., Jiang, S., Yang, H., Guo, J., Jiang, L.Y., Li, T., Zhang, H., Bai, Y., Lou, Y., et al. (2023). Exhaustion-associated cholesterol deficiency dampens the cytotoxic arm of antitumor immunity. Cancer Cell *41*, 1276–1293.e11. https://doi.org/10.1016/j.ccell.2023.04.016.

63. Mellman, I., Chen, D.S., Powles, T., and Turley, S.J. (2023). The cancer-immunity cycle: Indication, genotype, and immunotype. Immunity *56*, 2188–2205. https://doi.org/10.1016/j.immuni.2023.09.011.

64. Galassi, C., Chan, T.A., Vitale, I., and Galluzzi, L. (2024). The hallmarks of cancer immune evasion. Cancer Cell *42*, 1825–1863. https://doi.org/10.1016/j.ccell.2024.09.010.

65. Jain, R.K. (2001). Normalizing tumor vasculature with anti-angiogenic therapy: a new paradigm for combination therapy. Nat. Med. *7*, 987–989. https://doi.org/10.1038/nm0901-987.

66. Fassnacht, M., Berruti, A., Baudin, E., Demeure, M.J., Gilbert, J., Haak, H., Kroiss, M., Quinn, D.I., Hesseltine, E., Ronchi, C.L., et al. (2015). Linsitinib (OSI-906) versus placebo for patients with locally advanced or metastatic adrenocortical carcinoma: a double-blind, randomised, phase 3 study. Lancet Oncol. *16*, 426–435. https://doi.org/10.1016/S1470-2045(15)70081-1.

67. Gide, T.N., Quek, C., Menzies, A.M., Tasker, A.T., Shang, P., Holst, J., Madore, J., Lim, S.Y., Velickovic, R., Wongchenko, M., Yan, Y., et al. (2019). Distinct Immune Cell Populations Define Response to Anti-PD-1 Monotherapy and Anti-PD-1/Anti-CTLA-4 Combined Therapy. Cancer Cell *35*, 238–255.e6. https://doi.org/10.1016/j.ccell.2019.01.003.

68. Subramanian, A., Nemat-Gorgani, N., Ellis-Caleo, T.J., van, D.G.P., Sears, T.J., Somani, A., Luca, B.A., Zhou, M.Y., Bradic, M., Torres, I.A., Oladipo, E., et al. (2024). Sarcoma microenvironment cell states and ecosystems are associated with prognosis and predict response to immunotherapy. Nat. Cancer *5*, 642–658. https://doi.org/10.1038/s43018-024-00743-y.

69. Kumar, V., Ramnarayanan, K., Sundar, R., Padmanabhan, N., Srivastava, S., Koiwa, M., Yasuda, T., Koh, V., Huang, K.K., Tay, S.T., et al. (2022). Single-Cell Atlas of Lineage States, Tumor Microenvironment, and Subtype-Specific Expression Programs in Gastric Cancer. Cancer Discov. *12*, 670–691. https://doi.org/10.1158/2159-8290.CD-21-0683.

70. Tran, M.A., Youssef, D., Shroff, S., Chowhan, D., Beaumont, K.G., Sebra, R., Mehrazin, R., Wiklund, P., Lin, J.J., Horowitz, A., et al. (2024). Urine scRNAseq reveals new insights into the bladder tumor immune microenvironment. J. Exp. Med. *221*, e20240045. https://doi.org/10.1084/jem.20240045.

71. Salomé, B., Sfakianos, J.P., Ranti, D., Daza, J., Bieber, C., Charap, A., Hammer, C., Banchereau, R., Farkas, A.M., Ruan, D.F., et al. (2022). NKG2A and HLA-E define an alternative immune checkpoint axis in bladder cancer. Cancer Cell *40*, 1027–1043.e9. https://doi.org/10.1016/j.ccell.2022.08.005.

72. Wu, S.Z., Al-Eryani, G., Roden, D.L., Junankar, S., Harvey, K., Andersson, A., Thennavan, A., Wang, C., Torpy, J.R., Bartonicek, N., et al. (2021). A single-cell and spatially resolved atlas of human breast cancers. Nat. Genet. *53*, 1334–1347. https://doi.org/10.1038/s41588-021-00911-1.

73. Wu, F., Fan, J., He, Y., Xiong, A., Yu, J., Li, Y., Zhang, Y., Zhao, W., Zhou, F., Li, W., et al. (2021). Single-cell profiling of tumor heterogeneity and the microenvironment in advanced non-small cell lung cancer. Nat. Commun. *12*, 2540. https://doi.org/10.1038/s41467-021-22801-0.

Please cite this article in press as: Wang et al., A blood-brain barrier-like vascular gate limits immunotherapy efficacy in neuroendocrine cancers, Cell (2026), https://doi.org/10.1016/j.cell.2026.04.017

74. Lee, H.O., Hong, Y., Etlioglu, H.E., Cho, Y.B., Pomella, V., Van den Bosch, B., Vanhecke, J., Verbandt, S., Hong, H., Min, J.W., et al. (2020). Lineage-dependent gene expression programs influence the immune landscape of colorectal cancer. Nat. Genet. *52*, 594–603. https://doi.org/10.1038/s41588-020-0636-z.

75. Yang, Y., Li, Y., Yu, H., Ding, Z., Chen, L., Zeng, X., He, S., Liao, Q., Zhao, Y., and Yuan, Y. (2023). Comprehensive landscape of resistance mechanisms for neoadjuvant therapy in esophageal squamous cell carcinoma by single-cell transcriptomics. Signal Transduct. Target. Ther. *8*, 298. https://doi.org/10.1038/s41392-023-01518-0.

76. Shi, H., Tian, H., Zhu, T., Liao, Q., Liu, C., Yuan, P., Li, Y., Yang, J., Zong, C., Jia, S., et al. (2024). Single-cell sequencing depicts tumor architecture and empowers clinical decision in metastatic conjunctival melanoma. Cell Discov. *10*, 63. https://doi.org/10.1038/s41421-024-00683-y.

77. Lauss, M., Phung, B., Borch, T.H., Harbst, K., Kaminska, K., Ebbesson, A., Hedenfalk, I., Yuan, J., Nielsen, K., Ingvar, C., et al. (2024). Molecular patterns of resistance to immune checkpoint blockade in melanoma. Nat. Commun. *15*, 3075. https://doi.org/10.1038/s41467-024-47425-y.

78. Tirosh, I., Izar, B., Prakadan, S.M., Wadsworth, M.H., 2nd, Treacy, D., Trombetta, J.J., Rotem, A., Rodman, C., Lian, C., Murphy, G., et al. (2016). Dissecting the multicellular ecosystem of metastatic melanoma by single-cell RNA-seq. Science *352*, 189–196. https://doi.org/10.1126/science.aad0501.

79. Huang, Y.J., Cao, D.Y., Zhang, M.X., Yang, Y., Niu, G.M., Tang, L.A., Shen, Z., Zhang, Z.C., Bai, Y.Q., Min, D.L., et al. (2024). Exploring the impact of PDGFD in osteosarcoma metastasis through single-cell sequencing analysis. Cell. Oncol. *47*, 1715–1733. https://doi.org/10.1007/s13402-024-00949-3.

80. Su, C., Lv, Y., Lu, W., Yu, Z., Ye, Y., Guo, B., Liu, D., Yan, H., Li, T., Zhang, Q., et al. (2021). Single-Cell RNA Sequencing in Multiple Pathologic Types of Renal Cell Carcinoma Revealed Novel Potential Tumor-Specific Markers. Front. Oncol. *11*, 719564. https://doi.org/10.3389/fonc.2021.719564.

81. Yu, Z., Lu, W., Su, C., Lv, Y., Ye, Y., Guo, B., Liu, D., Yan, H., Mi, H., Li, T., et al. (2021). Single-Cell RNA-seq Identification of the Cellular Molecular Characteristics of Sporadic Bilateral Clear Cell Renal Cell Carcinoma. Front. Oncol. *11*, 659251. https://doi.org/10.3389/fonc.2021.659251.

82. Cancer Genome Atlas Research Network. Author Correction: Comprehensive molecular profiling of lung adenocarcinoma. Nature. 2018;559:E12. https://doi.org/10.1038/s41586-018-0228-6. Erratum for: Nature. 2014;511:543-50. https://doi.org/10.1038/nature13385.

83. Hieronymus, H., Schultz, N., Gopalan, A., Carver, B.S., Chang, M.T., Xiao, Y., Heguy, A., Huberman, K., Bernstein, M., Assel, M., Murali, R., et al. (2014). Copy number alteration burden predicts prostate cancer relapse. Proc. Natl. Acad. Sci. USA *111*, 11139–11144. https://doi.org/10.1073/pnas.1411446111.

84. Dobin, A., Davis, C.A., Schlesinger, F., Drenkow, J., Zaleski, C., Jha, S., Batut, P., Chaisson, M., Gingeras, T.R., et al. (2013). STAR: ultrafast universal RNA-seq aligner. Bioinformatics *29*, 15–21. https://doi.org/10.1093/bioinformatics/bts635.

85. Love, M.I., Huber, W., and Anders, S. (2014). Moderated estimation of fold change and dispersion for RNA-seq data with DESeq2. Genome Biol. *15*, 550. https://doi.org/10.1186/s13059-014-0550-8.

86. Hänzelmann, S., Castelo, R., and Guinney, J. (2013). GSVA: gene set variation analysis for microarray and RNA-seq data. BMC Bioinformatics *14*, 7. https://doi.org/10.1186/1471-2105-14-7.

87. Korsunsky, I., Millard, N., Fan, J., Slowikowski, K., Zhang, F., Wei, K., Baglaenko, Y., Brenner, M., Loh, P.R., and Raychaudhuri, S. (2019). Fast, sensitive and accurate integration of single-cell data with Harmony. Nat. Methods *12*, 1289–1296. https://doi.org/10.1038/s41592-019-0619-0.

88. Ritchie, M.E., Phipson, B., Wu, D., Hu, Y., Law, C.W., Shi, W., and Smyth, G. (2015). limma powers differential expression analyses for RNA-sequencing and microarray studies. Nucleic Acids Research *43*, e47. https://doi.org/10.1093/nar/gkv007.

89. Browaeys, R., Saelens, W., and Saeys, Y. (2020). NicheNet: modeling intercellular communication by linking ligands to target genes. Nature Methods *17*, 159–162. https://doi.org/10.1038/s41592-019-0667-5.

90. Butler, A., Hoffman, P., Smibert, P., Papalexi, E., and Satija, R. (2018). Integrating single-cell transcriptomic data across different conditions, technologies, and species. Nat. Biotechnol. *36*, 411–420. https://doi.org/10.1038/nbt.4096.

91. Alexa, A., Rahnenführer, J., and Lengauer, T. (2006). Improved scoring of functional groups from gene expression data by decorrelating GO graph structure. Bioinformatics *22*, 1600–1607. https://doi.org/10.1093/bioinformatics/btl140.

92. Chu, T., Wang, Z., Pe'er, D., and Danko, C.G. (2022). Cell type and gene expression deconvolution with BayesPrism enables Bayesian integrative analysis across bulk and single-cell RNA sequencing in oncology. Nat. Cancer *3*, 505–517. https://doi.org/10.1038/s43018-022-00356-3.

93. Chen, J., Dai, S., Zhao, L., Peng, Y., Sun, C., Peng, H., Zhong, Q., Quan, Y., Li, Y., Chen, X., et al. (2023). A New Type of Endometrial Cancer Models in Mice Revealing the Functional Roles of Genetic Drivers and Exploring their Susceptibilities. Adv. Sci. *10*, e2300383. https://doi.org/10.1002/advs.202300383.

94. Schupp, J.C., Adams, T.S., Cosme, C., Jr., Raredon, M.S.B., Yuan, Y., Omote, N., Poli, S., Chioccioli, M., Rose, K.A., Manning, E.P., et al. (2021). Integrated Single-Cell Atlas of Endothelial Cells of the Human Lung. Circulation *144*, 286–302. https://doi.org/10.1161/CIRCULATIONAHA.120.052318.

95. Zheng, X., Wang, X., Cheng, X., Liu, Z., Yin, Y., Li, X., Huang, Z., Wang, Z., Guo, W., Ginhoux, F., et al. (2023). Single-cell analyses implicate ascites in remodeling the ecosystems of primary and metastatic tumors in ovarian cancer. Nat. Cancer *4*, 1138–1156. https://doi.org/10.1038/s43018-023-00599-8.

96. Lu, Y., Yang, A., Quan, C., Pan, Y., Zhang, H., Li, Y., Gao, C., Lu, H., Wang, X., Cao, P., et al. (2022). A single-cell atlas of the multicellular ecosystem of primary and metastatic hepatocellular carcinoma. Nat. Commun. *13*, 4594. https://doi.org/10.1038/s41467-022-32283-3.

Please cite this article in press as: Wang et al., A blood-brain barrier-like vascular gate limits immunotherapy efficacy in neuroendocrine cancers, Cell (2026), https://doi.org/10.1016/j.cell.2026.04.017

STAR★METHODS

KEY RESOURCES TABLE

REAGENT or RESOURCE	SOURCE	IDENTIFIER
Antibodies		
Anti-MASH1/Achaete-scute homolog 1 antibody	Abcam	Cat# ab211327; RRID: AB_2924270
Anti-PDGFR beta antibody	Abcam	Cat# ab69506; RRID: AB_1269704
Anti-Collagen IV antibody	Abcam	Cat# ab6586; RRID: AB_305584
Anti-CD3 antibody	Abcam	Cat# ab11089; RRID: AB_2889189
Anti-mCherry antibody	Abcam	Cat# ab125096; RRID: AB_11133266
Goat Anti-Rat IgG H&L (Cy3 ®) preadsorbed	Abcam	Cat# ab98416; RRID: AB_10673341
IGFBP5 Polyclonal antibody	Proteintech	Cat# 55205-1-AP; RRID: AB_2736835
Anti-alpha smooth muscle Actin Rabbit pAb	Servicebio	Cat# GB111364; RRID: AB_2910228
Anti-CD31 Mouse mAb	Servicebio	Cat# GB12063; RRID: AB_2941868
Anti-CD31 Rabbit pAb	Servicebio	Cat# GB11063; RRID: AB_2922436
Anti -IGF-1 Rabbit pAb	Servicebio	Cat# GB11248; RRID: AB_3644255
Anti-IGF1 Receptor Rabbit pAb	Servicebio	Cat# GB115049
Anti-CD3 Rabbit pAb	Servicebio	Cat# GB13014; RRID: AB_2920578
Laminin beta 1 Recombinant Rabbit Monoclonal Antibody	HuaBio	Cat# ET1703-14; RRID: AB_3070371
CD4 Rabbit Polyclonal Antibody	HuaBio	Cat# 0108-6; RRID: AB_3068634
ZO-1 Monoclonal Antibody (ZO1-1A12)	Thermo Fisher Scientific	Cat# 33-9100; RRID: AB_87181
CD8α XP® Rabbit	Cell Signaling Technology	Cat# 98941; RRID: AB_2756376
HRP-conjugated actin antibody	Thermo Fisher Scientific	Cat# MA5–32540; RRID: AB_2809817
Anti-Mouse CD45.2	BioLegend	Cat #109831; RRID: AB_2565511
Anti-mouse CD31 Antibody	BioLegend	Cat #102410; RRID: AB_312905
Bacterial and virus strains		
DH5α	N/A	TSV-A07
Biological samples	N/A	N/A
Mouse sample	This paper	N/A
Human lung samples	West China Hospital	N/A
Chemicals, peptides, and recombinant proteins		
DMEM/F-12, HEPES	Gibco	Cat#C11330500BT
Dulbecco's Modified Eagle Medium	Gibco	Cat#C11995500BT
Penicillin/Streptomycin	Gibco	Cat# 15140-122
GlutaMAX Supplement	Gibco	Cat# 35050-061
B-27 Plus Supplement	Gibco	Cat#A3582801
N-2 Supplement	Gibco	Cat#17502048
N-Acetyl-L-cysteine	Sigma	Cat# A9165
Nicotinamide	Sigma	Cat# N0636
Human EGF, animal-free recombinant protein	PeproTech	Cat# AF-100-15
Noggin	PeproTech	Cat# 120-10C
Human FGF-10 recombinant protein	PeproTech	Cat#100-26
R-Spondin-1	PeproTech	Cat#120-38
A83-01	BioGems	Cat#9094360
TrypLE Express Enzyme (1X), phenol red	Gibco	Cat#12605-028
Trypsin-EDTA (0.25%), phenol red	Gibco	Cat#25200-072

(*Continued on next page*)

Please cite this article in press as: Wang et al., A blood-brain barrier-like vascular gate limits immunotherapy efficacy in neuroendocrine cancers, Cell (2026), https://doi.org/10.1016/j.cell.2026.04.017

Continued

REAGENT or RESOURCE	SOURCE	IDENTIFIER
T7 Endonuclease I	Vazyme	Cat# EN303-01
Proteinase K	Solarbio	Cat# P9460
D-luciferin potassium salt	Biovision	Cat#7903-10PK
InVivoMAb anti-mouse PD-1	BioXcell	Cat# BE0273; RRID: AB_2687796
SIINFEKL	MedChemExpress	Cat# HY-P1489
anti-CD3 antibody	Biolegend	Cat# 100202; RRID: AB_312659
anti-CD28 antibodies	Biolegend	Cat# 102102; RRID: AB_312867
Recombinant Human IL-2	Novoprotein	Cat# GMP-CD66
Matrigel Matrix, phenol red-free, LDEV-free	Corning	Cat# 356237
TRIzol™ Reagent	Invitrogen	Cat#15596026
M-MLV reverse transcriptase	Invitrogen	Cat#28025013
PowerUp™ SYBR™ Green Master Mix	Applied Biosystems	Cat#A25741
Dimethyl sulfoxide	MPbio	Cat#196055
DPBS, no calcium, no magnesium	Gibco	Cat# C14190500BT
Collagenase I	Gibco	Cat#17100-017
Collagenase IV	Gibco	Cat#17104-019
Linsitinib (OSI-906)	Selleckchem	Cat# S1091
Evan's blue	Yeasen	Cat# 314-13-6
Fetal bovine serum	Multicell	Cat# 086-150
IRISKit™ HyperView mTSA Kit	LUMINIRIS Bio Tech	Cat #MH900206
Lycopersicon esculentum (Tomato) lectin (LEL/TL), DyLight 649	Vector Laboratories	Cat# DL-1178-1
SNARF-4F 5-(and-6)-carboxylic acid	Invitrogen	Cat# S23920
Critical commercial assays		
Chromium™ Single Cell 3' Library & Gel Bead Kit v3.1	10x Genomics	Cat # PN-1000121
Deposited data		
EGAS00001005549 (immunotherapy cohort: muscle-invasive bladder cancer)	Robertson et al.[24]	https://ega-archive.org/studies/EGAS00001005549
GSE176307 (immunotherapy cohort:urothelial cancer)	Rose et al.[23]	https://www.ncbi.nlm.nih.gov/geo/query/acc.cgi?acc=GSE176307
EGAD50000000243 (immunotherapy cohort:SCLC)	George et al.[32]	https://ega-archive.org/studies/EGAS50000000169
EGAD50000000195 (immunotherapy cohort:SCLC)	Nabet et al.[33]	https://ega-archive.org/datasets/EGAD50000000195
phs002822.v1.p1 (immunotherapy cohort:NSCLC)	Ravi et al.[22]	https://www.ncbi.nlm.nih.gov/projects/gap/cgi-bin/study.cgi?study_id=phs002822.v1.p1
GSE190265 (immunotherapy cohort:NSCLC)	Limagne et al.[30]	https://www.ncbi.nlm.nih.gov/geo/query/acc.cgi?acc=GSE190265
PRJNA482620 (immunotherapy cohort:GBM)	Zhao et al.[25]	http://tiger.canceromics.org/#/download
GSE78220 (immunotherapy cohort:melanoma)	Hugo et al.[26]	https://www.ncbi.nlm.nih.gov/geo/query/acc.cgi?acc=gse78220
GSE91061 (immunotherapy cohort:melanoma)	Riaz et al.[27]	https://www.ncbi.nlm.nih.gov/geo/query/acc.cgi?acc=GSE91061
GSE100797 (immunotherapy cohort:melanoma)	Lauss et al.[28]	https://www.ncbi.nlm.nih.gov/geo/query/acc.cgi?acc=GSE100797
phs000452.v3.p1 (immunotherapy cohort:melanoma)	Liu et al.[29]	https://www.ncbi.nlm.nih.gov/projects/gap/cgi-bin/study.cgi?study_id=phs000452.v3.p1
PRJEB23709 (immunotherapy cohort:melanoma)	Gide et al.[67]	http://tiger.canceromics.org/#/download
GSE213065 (immunotherapy cohort:SRC)	Subramanian et al.[68]	https://www.ncbi.nlm.nih.gov/geo/query/acc.cgi?acc=GSE213065

(*Continued on next page*)

Please cite this article in press as: Wang et al., A blood-brain barrier-like vascular gate limits immunotherapy efficacy in neuroendocrine cancers, Cell (2026), https://doi.org/10.1016/j.cell.2026.04.017

Continued

REAGENT or RESOURCE	SOURCE	IDENTIFIER
SCLC and NSCLC scRNA-seq	Chan et al.[6]	https://data.humantumoratlas.org
GSE183904 (gastric cancer scRNA-seq)	Kumar et al.[69]	https://www.ncbi.nlm.nih.gov/geo/query/acc.cgi?acc=GSE183904
GSE267718 (bladder cancer scRNA-seq)	Tran et al.[70]	https://www.ncbi.nlm.nih.gov/geo/query/acc.cgi?acc=GSE267718
Bladder cancer scRNA-seq	Salomé et al.[71]	https://data.mendeley.com/datasets/7yb7s9769c/1
Breast cancer scRNA-seq	Wu et al.[72,73]	https://singlecell.broadinstitute.org/single_cell/study/SCP1039
GSE132465 (colorectal cancer scRNA-seq)	Lee et al.[74]	https://www.ncbi.nlm.nih.gov/geo/query/acc.cgi?acc=GSE132465
GSE221561 (esophageal squamous cell carcinoma scRNA-seq)	Yang et al.[75]	https://www.ncbi.nlm.nih.gov/geo/query/acc.cgi?acc=GSE221561
GSE217707 (melanoma scRNA-seq)	Shi et al.[76]	https://www.ncbi.nlm.nih.gov/geo/query/acc.cgi?acc=GSE217707
GSE244983 (melanoma scRNA-seq)	Lauss et al.[77]	https://www.ncbi.nlm.nih.gov/geo/query/acc.cgi?acc=GSE244983
GSE72056 (melanoma scRNA-seq)	Tirosh et al.[78]	https://www.ncbi.nlm.nih.gov/geo/query/acc.cgi?acc=GSE72056
GSE250015 (osteosarcoma scRNA-seq)	Huang et al.[79]	https://www.ncbi.nlm.nih.gov/geo/query/acc.cgi?acc=GSE250015
GSE152938 (renal cell carcinoma scRNA-seq)	Su et al.[80]	https://www.ncbi.nlm.nih.gov/geo/query/acc.cgi?acc=GSE152938
GSE171306 (renal cell carcinoma scRNA-seq)	Yu et al.[81]	https://www.ncbi.nlm.nih.gov/geo/query/acc.cgi?acc=GSE171306
EGAD00001001244 (SCLC bulk RNA-seq)	George et al.[45]	https://ega-archive.org/datasets/EGAD00001001244
HRA003419 (SCLC bulk RNA-seq)	Liu et al.[9]	https://ngdc.cncb.ac.cn/gsa-human/browse/HRA003419
TCGA-LUAD bulk RNA-seq	Cancer Genome Atlas Research Network[82]	https://portal.gdc.cancer.gov/projects/TCGA-LUAD
OMIX002489 (SCLC proteomic data)	Liu et al.[9]	https://ngdc.cncb.ac.cn/omix/release/OMIX002489
GSE155690 (ASCL1 ChIP data)	Olsen et al.[49]	https://www.ncbi.nlm.nih.gov/geo/query/acc.cgi?acc=GSE155690
GSE155691 (Ascl1 KO vs Ascl1 WT bulk RNA-seq)	Olsen et al.[49]	https://www.ncbi.nlm.nih.gov/geo/query/acc.cgi?acc=GSE155691
GSE98894 (panneuroendocrine cancer bulk RNA-seq)	Alvarez et al.[59]	https://www.ncbi.nlm.nih.gov/geo/query/acc.cgi?acc=GSE98894
Castration-resistant neuroendocrine prostate cancer bulk RNA-seq	Beltran et al.[60]	https://www.cbioportal.org/study?id=nepc_wcm_2016
Prostate cancer bulk RNA-seq	Hieronymus et al.[83]	https://www.cbioportal.org/study?id=prad_mskcc_2014
Castration-resistant neuroendocrine prostate cancer scRNA-seq	Chan et al.[3]	https://www.ncbi.nlm.nih.gov/geo/query/acc.cgi?acc=GSE210358
Sequencing data in this study	This paper	https://www.ncbi.nlm.nih.gov/geo/query/acc.cgi?acc=GSE287964
Experimental models: Cell lines		
Human: SHP-77	ATCC	#CRL-2195; RRID: CVCL_1693
Human: NCI-H526	ATCC	#CRL-5811; RRID: CVCL_1569
Human: HEK-293T	ATCC	#CRL-3216; RRID: CVCL_0063
Human: A549	ATCC	#CCL-185; RRID: CVCL_0023

(*Continued on next page*)

Please cite this article in press as: Wang et al., A blood-brain barrier-like vascular gate limits immunotherapy efficacy in neuroendocrine cancers, Cell (2026), https://doi.org/10.1016/j.cell.2026.04.017

Continued

REAGENT or RESOURCE	SOURCE	IDENTIFIER
Experimental models: Organisms/strains		
Mouse:sg*Trp53*;Kras^{G12D};*Myc*;	Chen-Liu laboratory	See STAR Methods
Mouse:sg*Trp53*;sg*Rb1*;Myc;	Chen-Liu laboratory	See STAR Methods
Mouse:CAG-Cas9-EGFP	Jackson Lab	Cat# JAX:026179
Mouse: C57BL/6-Tg (TcraTcrb) 1100Mjb/J	GemPharmatech	Cat# N000013
Oligonucleotides		
CRISPR sgRNA for *Ascl1*, *Igfbp5*, *Igf1r* see Table S7	This paper	https://www.atum.bio/eCommerce/cas9/input
RT-qPCR primer, see Table S7	This paper	https://pga.mgh.harvard.edu/primerbank/index.html
Recombinant DNA		
V2TC-sgRNA	This paper	N/A
PIL-Myc-Luci2	This paper	N/A
Software and algorithms		
Cellranger v7.0.1	10x Genomics	https://support.10xgenomics.com/single-cell-gene-expression/software/pipelines/latest/using/count#cr-count
STAR v2.6.0	Dobin et al.[84]	https://github.com/alexdobin/STAR
DESeq2 v1.46.0	Love et al.[85]	https://github.com/thelovelab/DESeq2
GSVA v2.0.7	Hänzelmann et al.[86]	https://github.com/rcastelo/GSVA
harmony v1.2.4	Korsunsky et al.[87]	https://github.com/immunogenomics/harmony
limma v3.62.2	Ritchie et al.[88]	https://cran.r-project.org/src/contrib/Archive/limma/
nichenetr v2.2.0	Browaeys et al.[89]	https://github.com/saeyslab/nichenetr
Seurat v4.3.0	Butler et al.[90]	https://github.com/satijalab/seurat
survival v3.8.3	CRAN Repository	https://cran.r-project.org/web/packages/survival/index.html
survminer v0.5.1	CRAN Repository	https://cran.r-project.org/web/packages/survminer/index.html
sva v3.54.0	Leek et al., 2012	https://bioconductor.org/packages/release/bioc/html/sva.html
topGO v2.58.0	Alexa et al.[91]	https://bioconductor.org/packages/release/bioc/html/topGO.html
clusterProfiler v4.14.6	Bioconductor	https://bioconductor.org/packages/release/bioc/html/clusterProfiler.html
ComplexHeatmap v2.22.0	Bioconductor	https://bioconductor.org/packages/release/bioc/html/ComplexHeatmap.html
pheatmap v1.0.13	CRAN Repository	https://cran.r-project.org/web/packages/pheatmap/index.html
ggplot2 v4.0.0	CRAN Repository	https://cran.r-project.org/web/packages/ggplot2/index.html
ggpubr v0.6.2	CRAN Repository	https://cran.r-project.org/web/packages/ggpubr/index.html
BayesPrism v2.2.2	Chu et al.[92]	https://github.com/Danko-Lab/BayesPrism
Code generated for this study	This paper	GitHub: https://github.com/AilingZhong/SCLC_ICI_Project; Zenodo: https://doi.org/10.5281/zenodo.19186885

METHOD DETAILS

Mice

All animal experiments were conducted following protocols approved by the Institutional Animal Care and Use Committee of Sichuan University. The mouse strains used in this study included CGAS-Cas9-EGFP mice (Male, Jackson Lab, Cat# JAX:026179), C57BL/6JGpt (Male, GemPharmatech Co., Ltd, Cat# N000013), BALB/cNj-Foxn1nu/Gpt (Male, GemPharmatech Co., Ltd, Cat# D000521), and C57BL/6-Tg (TcraTcrb)1100Mjb/J (OT-1) (Male, Jackson Lab, Cat# JAX:003831). All mice were 6-8 weeks old, with an average body weight of 20 g at the start of experiments. The animals were maintained in a specific pathogen-free (SPF) facility at Sichuan University. The housing conditions included autoclaved food, bedding, and water, with environmental controls set to maintain a temperature of 23 ± 2°C and relative humidity of 30-70%. The light cycle was regulated to a 12-hour light/12-hour dark schedule (6:00–18:00).

Human specimens

This study was approved by the Ethical Research Committee of West China Hospital (Approval Nos. 2023-987 and 2024-147). Written informed consent was obtained from all participants before the start of any study-related procedures. Certified pathologists at West China Hospital pathologically confirmed all tumor samples. Sample collection was conducted following standard clinical practice protocols. The demographic characteristics and relevant clinical data of the patients included in this study are detailed in Table S5.

Cell line

A549 (#CCL-185), SHP-77 (#CRL-2195), NCI-H526 (#CRL-5811) and HEK293T (#CRL-3216) cells were obtained from the American Type Culture Collection (ATCC). Cells were cultured following the ATCC instructions.

Organoid culture

The method for culturing tumor/normal organoids was performed as previously described.[34] In brief, tumor tissues were dissected into 5 mm^3 pieces and incubated in a digestion buffer containing 1.0 mg/ml collagenase I (Gibco, Cat#17100-017) and 0.5 mg/ml collagenase IV (Gibco, Cat#17104-019) in DMEM/F-12, HEPES (Gibco, Cat#C11330500BT). The tissues were mechanically pipetted at 10-minute intervals and gently agitated at 37°C for 30 minutes. Subsequently, the resulting mixture was filtered through 100 μm cell strainers. Following red blood cell lysis with ammonium-chloride-potassium (ACK) lysis buffer, 1×10^5 cells were resuspended in 30μl ice-cold Matrigel Matrix, phenol red-free, LDEV-free (Corning, Cat# 356237) and plated into a 48-well tissue culture plate. The lung organoid medium was prepared according to established protocols. The organoids were cultured at 37°C with 5% CO_2 and were passaged every 2-3 days using TrypLE™ Express Enzyme (1X), phenol red (Gibco, Cat# 12605-028) to ensure proper dissociation and continuous growth.

Isolation and Sorting of Endothelial Cells (ECs) from Tumor/Normal Tissues

Mouse tumor or normal lung tissues expressing Cas9 were dissociated using a digestion buffer containing 1.0 mg/mL collagenase I and 0.5 mg/mL collagenase IV in DMEM/F12 medium. For bulk RNA-seq, after dissociation, endothelial cells (ECs) were sorted as $GFP^-CD45^-CD31^+$ populations using flow cytometry. For Cas9-expressing normal endothelial cell culture, after enzymatic dissociation, endothelial cells were isolated using a magnetic cell-sorting system with CD31 MicroBeads, mouse (Miltenyi Biotec, Cat# 130-097-418). Before CD31 labeling, $CD45^+$ cells were depleted using a $CD45^+$ depletion kit (Miltenyi Biotec, Cat# 130-052-301). All procedures were conducted following the manufacturer's protocol. The sorted $CD31^+$ cells were plated on 0.1% gelatin (Sigma, Cat# G1393)-coated culture plates and maintained in the endothelial growth medium EGM-2 Endothelial Cell Growth Medium-2 BulletKit (Lonza, Cat# CC-3162). After several days of culture and expansion, endothelial cells were directly subjected to flow cytometry for expression analysis without passaging. Normal endothelial cells were then infected and mixed with SCLC tumor cells at a 1:1 ratio (1×10^5 cells: 1×10^5 cells) for subcutaneous transplantation.

Gene editing

Single-guide RNAs (sgRNAs) were designed using the CRISPR Design Tool (https://www.atum.bio/eCommerce/cas9/input) and subsequently cloned into the lentiviral vector V2TC, which facilitates bicistronic expression of both sgRNA and mCherry. The sgRNAs and PCR sequences utilized in this study are provided in Table S7. Lentivirus packaging and infection were performed as previously reported.[34] Briefly, after dissociation with TrypLE™, cells were mixed with lentivirus carrying the sgRNAs, centrifuged at 2000 rpm for 1 hour, and then incubated for 1.5 hours at 37°C in a 5% CO_2 atmosphere. Following infection, the cells were resuspended in ice-cold Matrigel and seeded into a 48-well tissue culture plate for further culture.

Mouse models generation

Primary orthotopic mouse models for multiple cancer types, including lung cancer, esophageal cancer, endometrial cancer, gastric cancer, and bladder cancer, have been established in our laboratory as previously reported.[34,38–41,93] For instance, the non-small cell lung cancer (NSCLC) mouse model was generated by injecting mouse normal lung organoids derived from CGAS-Cas9-EGFP mice (carrying *Trp53* mutation, *Myc*, and $Kras^{G12D}$ amplification) into the left lung of C57BL/6 mice. Before injection, gene-edited organoids were digested with TrypLE™ at 37°C for 10 minutes and centrifuged at 400 g for 5 minutes. The collected cells were resuspended in 50% Matrigel. 1×10^5 cells in a 50μl volume were injected into the left lung of C57BL/6 mice (male, 6-8 weeks, ~20g) using an insulin syringe following anesthesia induction.

Please cite this article in press as: Wang et al., A blood-brain barrier-like vascular gate limits immunotherapy efficacy in neuroendocrine cancers, Cell (2026), https://doi.org/10.1016/j.cell.2026.04.017

In vivo treatment

A total of 1 × 10^5 SCLC tumor cells were suspended in 100 μL of 50% Matrigel and subcutaneously implanted into mice for each transplantation. Tumor growth was monitored at 3-day intervals for up to 21 days. Tumor length (L) and width (W) were measured using a vernier caliper, and tumor volume was calculated using the formula: tumor volume = $(L \times W^2)/2$. For immunotherapy, when the average tumor volume reached approximately 100 mm^3, mice were randomized to receive either vehicle alone or anti-PD1 (BioXcell, Cat# BE0273) (100 μg per 20g body weight, administered every 3 days until sacrifice). For the combination treatment of IGF1R inhibitor Linsitinib (OSI-906) (Selleckchem, Cat# S1091) and immunotherapy, when the average tumor volume reached approximately 100 mm^3, mice were randomized into one of the following groups: (1) vehicle alone, (2) vehicle plus anti-PD1 (100 μg per 20g body weight, administered every 3 days until sacrifice), (3) vehicle plus IGF1R inhibitor (OSI-906, 25 mg/kg, administered 5 days per week via oral gavage), or (4) anti-PD1 plus OSI-906. OSI-906 was prepared in a solvent consisting of 5% DMSO, 40% PEG300, 5% Tween 80, and 50% ddH2O.

OT-1 T cell culture

Splenocytes from OT-1 mice were collected by mechanically dissociating the spleens through a 70μm cell strainer. The red blood cells were lysed with ammonium-chloride-potassium (ACK) lysis buffer for 1 minute on ice. The cells were then counted and resuspended at a concentration of 1 × 10^6 cells/mL in T cell complete medium consisting of RPMI supplemented with 10% fetal bovine serum, 2 mM L-glutamine, 1% penicillin-streptomycin, and 50 μM β-mercaptoethanol. The medium was further supplemented with 100 ng/mL $OVA^{257\text{-}264}$ peptide (SIINFEKL) (MedChemExpress, Cat# HY-P1489) and 100 U/mL human interleukin-2 (Novoprotein, Cat# GMP-CD66). The cells were seeded into a 6-well plate pre-coated with anti-mouse CD3 antibody (5 μg/mL; BioLegend, Cat# 100202) and anti-mouse CD28 antibody (1 μg/mL; BioLegend, Cat# 102102), which had been incubated overnight at 4°C. For in vivo experiments, 1 × 10^6 OT-I cells in 100 μL of suspension were intravenously (i.v.) injected into tumor-bearing mice. Seven days after the injection, the mice were euthanized, and tumor samples were collected for immunofluorescence staining.

RNA extraction and quantitative PCR

Total RNA was extracted using TRIzol™ Reagent (Invitrogen, Cat# 15596026) according to the manufacturer's instructions. Reverse transcription was subsequently carried out using M-MLV reverse transcriptase (Invitrogen, Cat# 28025013) following the provided protocol. RT–qPCR was performed with SYBR Green PCR Master Mix (Applied Biosystems, Cat# A25741) on a QuantStudio 3 Real-Time PCR System (Applied Biosystems). The relative expression levels of target genes were calculated using the 2-ΔΔCt method, with gene expression normalized to the housekeeping gene *Actb*/*Gapdh*. All primers used for qPCR analysis are listed in Table S7.

Intratumoral pH measurement

For tumor pH imaging, SNARF-4F 5-(and-6)-carboxylic acid (Invitrogen, Cat# S23920) was prepared as a 10μM working solution and administered according to the manufacturer's instructions and a previous study.[44] Tumors were then harvested and imaged using an IVIS system.

Doppler ultrasound imaging

Tumor blood flow was assessed using a Vevo 3100 high-frequency ultrasound imaging system. Mice bearing subcutaneous tumors were anesthetized with isoflurane and placed on a heated imaging platform. After hair removal and application of ultrasound gel, tumors were localized in B-mode. Intratumoral flow signals were identified by Power Doppler imaging, and pulsed-wave Doppler spectra were acquired at multiple sites within each tumor. The maximum blood flow velocity (Vmax) was calculated at each site from the Doppler spectral envelope, and the average Vmax across sites was used as the representative flow velocity for each tumor.

Tumor vascular perfusion assay

Vascular perfusion was analyzed via intravenous injection of 100 μL Lycopersicon esculentum (Tomato) lectin (LEL/TL), DyLight 649 (0.5 mg/mL, Vector Laboratories, Cat# DL-1178-1). Tissues were harvested 10 min later, embedded in Tissue-Tek O.C.T. Compound (Sakura Finetek, Cat# 4583), and cryosectioned. CD31 was detected by immunofluorescence staining for endothelial labeling and downstream perfusion analyses.

Spatial proteomics mass spectrometry approach

Spatial proteomics samples were prepared following a workflow involving sectioning, staining, imaging, laser capture microdissection (LCM), in-gel digestion, and mass spectrometry analysis. Tissue sections of 5 μm thickness from each biological sample were stained with H&E to identify tissue architecture and vascular regions, followed by imaging using a micro laser microdissection system (MMI) to isolate regions of interest. Liquid chromatography-tandem mass spectrometry (LC-MS/MS) was performed using the nanoElute system (Bruker Daltonics, Germany), coupled with the timsTOF Pro mass spectrometer (Bruker Daltonics, Germany) for data-independent acquisition (DIA). Mobile phases were composed of water with 0.1% formic acid (Phase A) and acetonitrile with 0.1%

Please cite this article in press as: Wang et al., A blood-brain barrier-like vascular gate limits immunotherapy efficacy in neuroendocrine cancers, Cell (2026), https://doi.org/10.1016/j.cell.2026.04.017

formic acid (Phase B). Reagents used were of mass spectrometry grade. For DIA acquisition, peptides were loaded onto a pre-column (5 mm × 300 μm i.d.) under 217.5 bar pressure, then separated on an analytical column (1.9 μm, 120 Å, 150 mm × 75 μm i.d.) at a flow rate of 300 nL/min, with a 60-minute gradient (0-50 min, 5% to 27% B; 50-60 min, 27% to 40% B).

Mass spectrometry parameters included a PASEF MS scan range of 100-1700 m/z, an ion mobility scan range of 0.7-1.3, and a ramp time of 166ms. Ion mobility peak detection threshold was set to 5,000, with 10 PASEF MS/MS scan events. A charge range of 0-5 was used, with a peak detection threshold of 2,500 cts/s across 56 windows.

Transmission electron microscope

For TEM, fresh tumor samples were immediately fixed with 2.5% glutaraldehyde and stored at 4°C. The Lilai Biomedicine Experiment Center prepared samples and captured photographs.

Determination of vascular permeability

To assess vascular permeability, 100μl 2% Evans blue (Yeasen Cat# 314-13-6) was intravenously injected into the mice. After 30 minutes, the mice were euthanized and intracardially perfused with Dulbecco's Phosphate Buffered Saline (DPBS), followed by 4% paraformaldehyde (PFA) to remove any residual dye from the blood vessels. The tumor samples were then collected and embedded in an Optimal Cutting Temperature (O.C.T.) compound (Tissue-Tek®, Sakura® Finetek, Cat# 4583). Cryosections (10 μm thick) were prepared, counterstained with anti-CD31 rabbit pAb (Servicebio Cat# GB11063-1-100) and DAPI (Beyotime Cat# P0131), and examined under a Nikon AXR Examiner with DAPI and Cyanine 3 (Cy3) and Cyanine 5 (Cy5) filter. Vascular permeability was quantified by measuring Evans blue intensity based on the Cy5 signal and analyzing the stained area using ImageJ and QuPath software.

H&E, immunohistochemistry, and immunofluorescence staining

Tumor sections with a thickness of 3μm were prepared from formalin-fixed paraffin-embedded (FFPE) samples. Deparaffinization was performed by immersing the sections in an eco-friendly dewaxing solution for 10 minutes twice. The sections were then rehydrated through a graded ethanol series (100%, 95%, and 75% ethanol) and finally rinsed in distilled water. Hematoxylin and eosin (H&E) staining was subsequently performed according to standard protocols.

For multiple immunohistochemistry (mIHC), the IRISKit™ HyperView mTSA Kit (Cat #MH900206) was utilized according to the manufacturer's instructions. Immunofluorescence (IF) staining was performed using fluorescence-conjugated secondary antibodies. Primary antibodies were diluted in 2% goat serum and incubated overnight at 4°C or room temperature, as specified in the manufacturer's instructions. Serial sections were prepared for vessel staining. In some experiments, sequential immunofluorescence staining was performed on the same tissue section or on consecutive serial sections to allow visualization of multiple markers while preserving spatial correspondence. After each round of staining and image acquisition, fluorescence signals were photobleached using the GEM Fluorescence Quenching System (model GEM10 SCI Pro, LUMINRIS) in combination with the IRISKit® Quench Buffer Kit (Cat# MH900105) for 10 min, and the same section was subsequently subjected to an additional round of staining and imaging. Imaging was performed and analyzed using a Nikon AXR Examiner and an Olympus VS200 microscope and the IRIS platform (https://irriss.com/) and QuPath software (version 0.5.1).

Analysis of the basement membrane thickness of tumor blood vessels

The thickness of the basement membrane of tumor blood vessels was measured using ImageJ software. For each tumor sample, three representative fields were selected for analysis. Within each field, the thickness of the basement membrane was measured at three distinct sections of each blood vessel, and the average thickness per vessel was calculated. The mean thickness of the blood vessels for each field was then determined by averaging the values obtained from all measured vessels within that field. Finally, the overall average basement membrane thickness for each tumor sample was calculated by averaging the mean thickness values from all three fields. This approach ensured a comprehensive and representative assessment of the basement membrane thickness across the tumor vasculature, and the analyses were conducted using ImageJ software.

Computational methods

Endothelial cell bulk RNA-seq analysis

Endothelial cells were isolated by flow cytometry and subjected to library preparation using the standard Illumina RNA library preparation protocol. Sequencing was performed on the Illumina NovaSeq 6000 platform. Reads were aligned to the mouse reference genome (mm10) using STAR (v2.6.0). Gene-level count matrices were analyzed with DESeq2 to obtain normalized counts, p values, and $\log_2$ fold changes. Transcriptional differences were visualized by volcano plots using an adjusted score derived from $\log_2$ fold change and mean gene expression.

Genes upregulated in SCLC-associated endothelial cells relative to NSCLC-associated endothelial cells were initially defined as those with $p < 0.05$ and $\log_2$ fold change > 0. To reduce potential contamination from other cell populations, these genes were further filtered against cell type-specific marker genes derived from published human SCLC scRNA-seq data.[6] Marker genes for malignant cells, normal epithelial cells, fibroblasts, myeloid cells, T cells, B cells, and plasma cells were identified using adjusted $p < 0.05$ and average $\log_2$ fold change > 0.1, converted to mouse ortholog symbols, and excluded from the endothelial upregulated gene set. The resulting filtered gene set was used for downstream functional enrichment analyses. GO enrichment analysis was performed using the enrichGO function in the clusterProfiler R package with org.Mm.eg.db as the annotation reference. Additional details are provided in Table S3.

Mouse scRNA-seq analysis

Single-cell RNA-seq libraries were generated using the Chromium Single Cell 3′ Reagent Kits v3 for sgIgfbp5 and sgScr SCLC tumors treated with anti-PD1 and/or OSI-906, and the Chromium Single Cell 5’ Reagent Kits for untreated sgIgfbp5 and sgScr SCLC tumors (10x Genomics), according to the manufacturer’s instructions. Libraries were sequenced on the Illumina NovaSeq X Plus platform. Custom reference genomes were generated by incorporating exogenous sequences, including sgRNA and Myc expression constructs, to enable discrimination between tumor and non-tumor cells. Reads were aligned to the GRCm38/mm10 mouse reference genome using Cell Ranger (v7.0.1). Subsequent analyses and visualization were performed using Seurat (v4.3.0). Datasets from different conditions were first combined using the Seurat “merge” function. Mitochondrial gene content was calculated using the “PercentageFeatureSet” function, and cells were filtered based on the following criteria: mitochondrial gene fraction < 20%, total RNA counts > 500, and 200-7,500 (or 8,500, depending on the sample) detected genes, as implemented in the available code. The filtered dataset was log-normalized using the “NormalizeData” function, and 2,500 highly variable genes were identified using the “FindVariableFeatures” function with the “vst” method. The data were then scaled and centered using the “ScaleData” function. Principal component analysis (PCA) was performed on the scaled expression matrix. To correct for batch effects across samples, Harmony was applied to the PCA embeddings. A shared nearest neighbor graph was constructed using the “FindNeighbors” function based on the top principal components, and clustering was performed using the “FindClusters” function at multiple resolutions (0.1-2.0). UMAP or openTSNE were used for dimensionality reduction and visualization based on the top principal components. Cell types were annotated according to canonical marker genes reported in previous studies (see Table S2). GSVA was performed to assess biological process activity. Additional details are provided in Table S2

T cell and tumor cell interaction analysis

Cell-cell communication analysis was performed using the iTALK R package. Gene expression matrices were extracted from Seurat objects and annotated with cell type and sample information. Mouse genes were converted to human orthologs before analysis. Highly expressed genes were identified using the “rawParse” function, and ligand-receptor pairs were predicted using the “FindLR” function across predefined categories, including growth factors, cytokines, immune checkpoints, and other signaling molecules. To enhance biological relevance, ligand-receptor pairs were further filtered based on cell type-specific differentially expressed genes. Only interactions supported by upregulated genes (adjusted p value < 0.01 and $\log_2$ fold change > 0) in each condition were retained for visualization.

Spatial proteomics mass spectrometry analysis

Spatial proteomics mass spectrometry data were analyzed using DIA-NN (v1.8.1). Protein inference was performed using protein names derived from a FASTA file. Library-free analysis was conducted with library generation based on protein IDs, retention time (RT), and ion mobility (IM) information. Robust LC-based quantification (high precision) was applied. The analysis was performed using a FASTA database (UP000000589_PD_mouse.fasta) containing 17,268 reviewed mouse proteins and contaminant proteins. Key parameters included fragment ion m/z ranging from 200 to 1,800, precursor m/z ranging from 300 to 1,800, and peptide lengths between 7 and 30 amino acids. Subsequently, normalized ion signal intensity values were used for downstream differential protein expression analysis, GO analysis, and GSEA (see Table S3). Proteomic differences were visualized by volcano plots using an adjusted score derived from $\log_2$ fold change and mean protein abundance. Additional details are provided in Table S3.

SCLC patient scRNAseq analysis

Single-cell RNA-seq libraries from 10 baseline SCLC samples in this study (Table S5) were generated using the Chromium Single Cell 5’ Reagent Kits v3 (10x Genomics), according to the manufacturer’s instructions. Count matrices were generated by Cell Ranger (v7.0.1) using the GRCh38 reference genome. Cells with mitochondrial gene fraction $\geq$ 20%, fewer than 200 or more than 10,000 detected genes, or total RNA counts $\leq$ 500 were excluded. The filtered dataset was log-normalized, and 2,500 highly variable genes were identified using the “vst” method. Data were scaled, followed by principal component analysis (100 PCs) and shared nearest neighbor graph construction based on the top 50 principal components. Cell types were annotated according to canonical marker gene expression. Patient-level classification into SCLC-A and SCLC-I subtypes was performed based on the proportions of tumor cells expressing *ASCL1*, *NEUROD1*, *POU2F3*, and *YAP1*, together with the extent of immune cell infiltration.

Clinical and public cohort analyses

SCLC cohort subtype classification and T cell infiltration analysis

Bulk RNA-seq data from 194 SCLC patient samples derived from the Liu et al.[9] and George et al.[45] cohorts were processed separately. For the Liu et al. cohort, samples annotated as “NAT-enriched” were excluded before analysis. Gene expression matrices from each cohort were centered and scaled using the “scale” function in R. The standardized expression values of *ASCL1*, *NEUROD1*, *POU2F3*, and *YAP1* were extracted, and SCLC subtypes were assigned by selecting the gene with the highest standardized expression in each sample. T cell proportions in each sample were estimated by deconvolution analysis using BayesPrism (Tables S2 and S7), using a single-cell reference expression matrix derived from Chan et al.[6]

Please cite this article in press as: Wang et al., A blood-brain barrier-like vascular gate limits immunotherapy efficacy in neuroendocrine cancers, Cell (2026), https://doi.org/10.1016/j.cell.2026.04.017

Pan-cancer endothelial cell scRNA-seq analysis

Endothelial single-cell transcriptomes were collected from normal lung tissues[94] and multiple cancer types, including gastric cancer,[69] ovarian cancer,[95] melanoma,[76–78] breast cancer,[72] bladder cancer,[70,71] esophageal carcinoma,[75] colorectal cancer,[74] hepatocellular carcinoma,[96] prostate cancer (GSE221603), renal cancer,[80,81] osteosarcoma,[79] lung squamous cell carcinoma,[73] lung adenocarcinoma,[6,73] and small cell lung cancer.[6] Endothelial cells from each group were extracted and averaged to generate pseudo-bulk expression profiles based on raw counts. GSVA was performed on the pseudo-bulk expression matrix using Gene Ontology (c5) gene sets. GSVA scores were visualized as heatmaps using the pheatmap package (see Table S3).

Definition of gene signatures

To define the SCLC BVG signature, pseudo-bulk endothelial expression profiles derived from pan-cancer endothelial scRNA-seq data were converted to counts per million (CPM). Genes enriched in SCLC endothelial cells were identified based on their higher expression relative to normal lung, LUAD, and pan-cancer endothelial cells. To reduce contamination from non-endothelial cell populations, genes annotated as markers of myeloid cells, T cells, or B/plasma cells in the Chan et al.[6] single cell dataset were excluded if they met the thresholds of adjusted p value < 0.05 and $\log_2$ fold change > 0. The remaining genes were defined as the SCLC BVG signature. The IGF1/IGF1R gene signature was compiled from several curated gene sets in the GSEA database (https://www.gsea-msigdb.org/). The signature included genes from the following pathways: KEGG_MEDICUS_REFERENCE_IGF2_IGF1R_PI3K_SIGNALING_PATHWAY, KEGG_MEDICUS_REFERENCE_IGF_IGF1R_RAS_ERK_SIGNALING_PATHWAY, KEGG_MEDICUS_REFERENCE_IGF_IGF1R_PI3K_SIGNALING_PATHWAY, IGF1R_TARGET_GENES, BIOCARTA_IGF1R_PATHWAY, BIOCARTA_IGF1_PATHWAY, and BIOCARTA_IGF1MTOR_PATHWAY. Further gene signature details are provided in Table S4.

BVG signature-based correlation analysis

Bulk RNA-seq data from SCLC cohorts reported by Liu et al. Liu et al.[9] and George et al.[45] were integrated and batch effect-corrected using the limma package. The corrected expression matrix was used for downstream analysis. The average expression of the BVG gene signature was calculated for each sample, and Spearman's correlation analysis was performed to evaluate the association between the BVG signature and individual genes across samples. An adjusted correlation score was calculated for each gene by integrating three components: the Spearman correlation coefficient with the BVG signature, the gene's overall expression abundance, and its differential expression ($\log_2$ fold change) between SCLC and NSCLC tumor cells. Genes were ranked based on this composite score. In addition, genes showing significant positive correlation with the BVG signature (Spearman's correlation coefficient > 0 and p value < 0.05) were retained for downstream analysis. Further gene signature details are provided in Table S4.

Identification of ASCL1-regulated genes associated with BVG signature

Since ASCL1 was identified as the top-ranked gene associated with the BVG signature, ChIP-seq-derived binding data and transcriptomic data from ASCL1 perturbation experiments were integrated (RNA-seq: *Ascl1* KO vs *Ascl1* WT: $\log_2$FoldChange < -2.5 & p-value < 0.05)[49] to further define downstream genes associated with ASCL1. Genes present in both datasets were further intersected with BVG signature-associated genes to identify candidate downstream targets. Further details are provided in Table S4.

T cell infiltration analysis in neuroendocrine tumor cohorts

Cell type proportions in each neuroendocrine tumor sample were estimated by deconvolution analysis using BayesPrism. GSVA was performed to assess biological process activity in each NEC patient (Table S6). The association between the GSVA score of "GO_ESTABLISHMENT_OF_ENDOTHELIAL_BARRIER" and T cell infiltration was visualized using smoothed curves generated with the ggplot2 package.

Pan-cancer immunotherapy cohort analysis

Overall survival (OS) benefit and objective response rate (ORR) benefit were defined as the differences between the ICB and control arms, calculated as median OS and ORR in the ICB arm minus those in the control arm, respectively. T cell infiltration levels in individual patients with available transcriptomic data were estimated using BayesPrism. GSVA was used to quantify the activity of immune- and endothelial-related pathways in each patient. In the SCLC IMpower133 cohort, subtype annotations were based on the Gay_MDACC_subtypes,[33] with classification criteria referenced from Gay et al.[8]

IMpower133 cohort survival analysis

For survival analysis, the average expression of BVG signature genes were calculated for each patient. To quantify the endothelial contribution to the BVG signature, this value was further weighted by the inferred endothelial cell fraction in each sample, and the resulting score was used for downstream survival analysis. In the IMpower133 cohort, 132 patients treated with chemo-immunotherapy were stratified into BVG-high and BVG-low groups using the optimal cut-point of the BVG score, determined by maximally selected rank statistics implemented in the survminer package (cut-point = 0.167). This cutoff yielded an approximate BVG^{high} to BVG^{low} ratio of 9:1. The 139 patients in the non-immunotherapy group were subsequently stratified using the same group ratio, and the association between BVG score and PFS was evaluated.

BVG signature expression in SCLC subtypes

Given the relatively high cancer-associated fibroblasts (CAFs) infiltration in the SCLC-I subtype of the IMpower133 cohort,[33] we sought to minimize the contribution of CAFs to the BVG signature score. To this end, the average expression of BVG signature genes was first calculated for each patient and then multiplied by "1-fibroblast fraction" to generate a CAF-adjusted BVG score, which was used to compare BVG signature levels across SCLC subtypes.

Please cite this article in press as: Wang et al., A blood-brain barrier-like vascular gate limits immunotherapy efficacy in neuroendocrine cancers, Cell (2026), https://doi.org/10.1016/j.cell.2026.04.017

QUANTIFICATION AND STATISTICAL ANALYSIS

Statistical significance in the figures is indicated as follows: $^{*}p < 0.05$, $^{**}p < 0.01$, $^{***}p < 0.001$, and $^{****}p < 0.0001$. Differences between groups were assessed using either a two-tailed unpaired Student's t test or the Mann–Whitney test. Correlations between variables were assessed using Spearman's correlation analysis. Comparisons of gene expression levels in scRNA-seq data were performed using the Wilcoxon rank-sum test or a two-sided unpaired Student's t test. Survival analyses were performed using the Kaplan-Meier method, with optimal cut-points determined by maximally selected rank statistics where indicated and significance assessed by the log-rank test. Statistical analyses were performed using GraphPad Prism (version 10; GraphPad Software) and R (v4.4.3). Statistical details for each experiment are provided in the corresponding figure legends and method details sections.

Supplemental figures

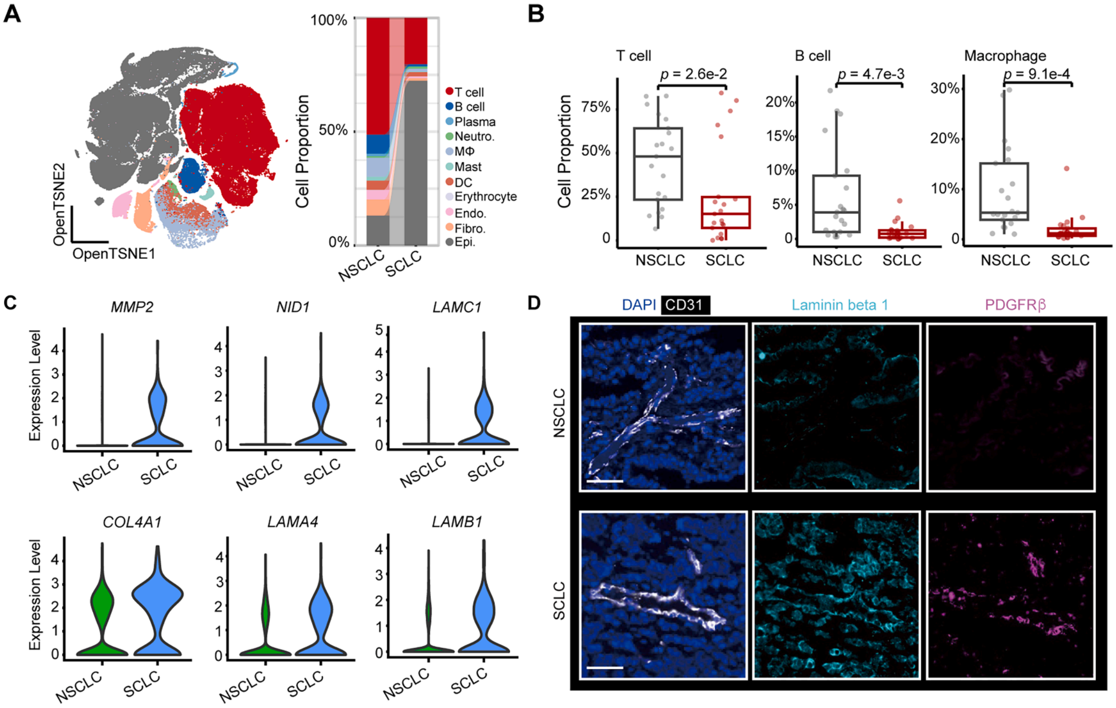

Figure S1. Additional features of the immunosuppressive SCLC microenvironment and its vasculature, related to Figure 1

(A) OpenTSNE embedding of single-cell transcriptomes from lung cancer patients (left). Alluvial plots illustrate differences in cell-type proportions between NSCLC and SCLC patients (right). Analysis is based on single-cell transcriptomic data from Chan et al.[6]

(B) Boxplots depict the proportions of infiltrating T cells, B cells, and macrophages in tumor tissues from NSCLC and SCLC patients, derived from scRNA-seq data reported by Chan et al.[6]

(C) Violin plots illustrate the expression levels of BM-associated genes in ECs from NSCLC and SCLC tumors, based on single-cell transcriptomic data from Chan et al.[6]

(D) Consecutive sections of NSCLC (left) and SCLC (right) tumor samples from patients were analyzed by IF for the expression of CD31, laminin beta 1, and PDGFRβ, as described in STAR Methods. Scale bars, 50 μm.

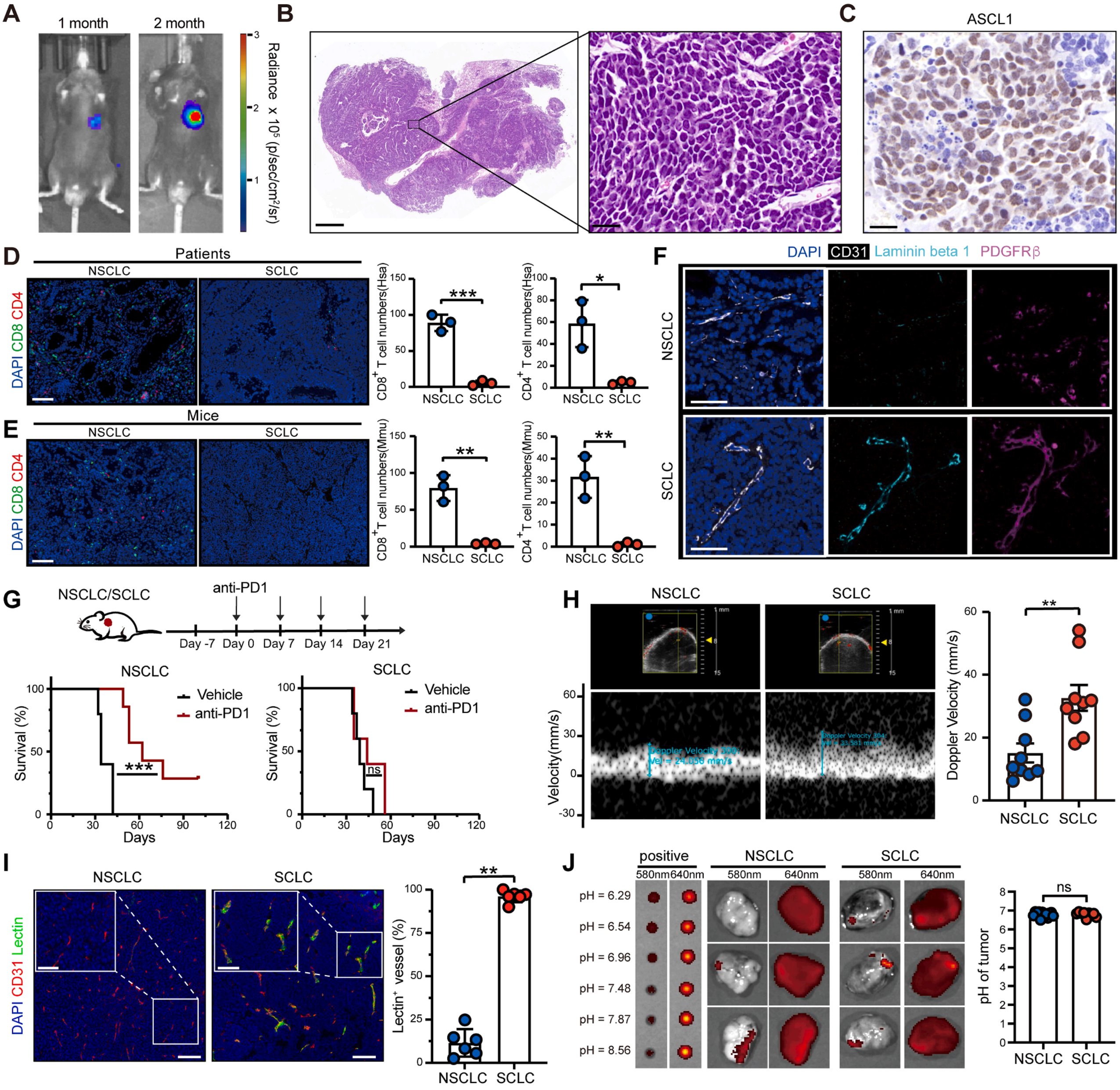

Figure S2. Additional characterization of the SCLC immune-excluding vasculature, related to Figure 2

(A) Representative bioluminescence images of the orthotopic SCLC mouse model during tumor progression.

(B) Representative H&E staining of a paraffin-embedded SCLC tumor sample from the mouse model. Scale bars, 500 μm; magnified region, 20 μm.

(C) IHC staining of ASCL1 in SCLC tumor samples from the SCLC mouse model. Scale bars, 20 μm.

(D) mIHC analysis of CD8 and CD4 in NSCLC and SCLC tumor samples from patients. Scale bars, 100 μm. Bar plots show the quantification of $CD8^+$ and $CD4^+$ T cells infiltrating the tissue. $^*p < 0.05$, $^{***}p < 0.001$. *t* test, mean ± SD of 3 biological replicate experiments.

(E) IF analysis of CD8 and CD4 in NSCLC and SCLC tumor samples from mice. Scale bars, 100 μm. Bar plots show the quantification of $CD8^+$ and $CD4^+$ T cells infiltrating the tissue. $^{**}p < 0.01$. *t* test, mean ± SD of 3 biological replicate experiments.

(F) Consecutive sections of NSCLC (up) and SCLC (down) tumor samples from mice were analyzed by IF for the expression of CD31, laminin beta 1, and PDGFRβ, as described in STAR Methods. Scale bars, 50 μm.

(G) Schematic of the immunotherapy treatment regimen in mouse models, and Kaplan-Meier survival curves of NSCLC and SCLC mouse models following immunotherapy. ns, not significant, $^{***}p < 0.001$.

(H) Representative Doppler ultrasound images showing measurement of intratumoral blood-flow velocity. Bar plots quantify peak Doppler velocity (Vmax) in NSCLC and SCLC tumors. $^{**}p < 0.01$, Mann-Whitney test. Data are shown as mean ± SEM from 9 biological replicates.

(I) Representative fluorescent images of lectin perfusion in NSCLC and SCLC tumor vessels. Scale bars, 100 μm. Magnified region, 50 μm. Bar plots quantify the $lectin^+$ vessels of NSCLC and SCLC tumors. $^{**}p < 0.01$. Mann-Whitney test. Mean ± SEM of 6 biological replicates.

(legend continued on next page)

(J) SNARF-4F exhibits pH-dependent dual-emission; the 580-nm and 640-nm channels were acquired, and their emission ratio (580/640) was used for ratiometric pH quantification. Representative fluorescence images of the positive control and NSCLC and SCLC tumors showing SNARF-4F-based pH detection. Bar plots quantify tumor pH in NSCLC and SCLC. ns, not significant; Mann-Whitney test. Data are shown as mean ± SEM with 12 biological replicates for NSCLC and 9 biological replicates for SCLC.

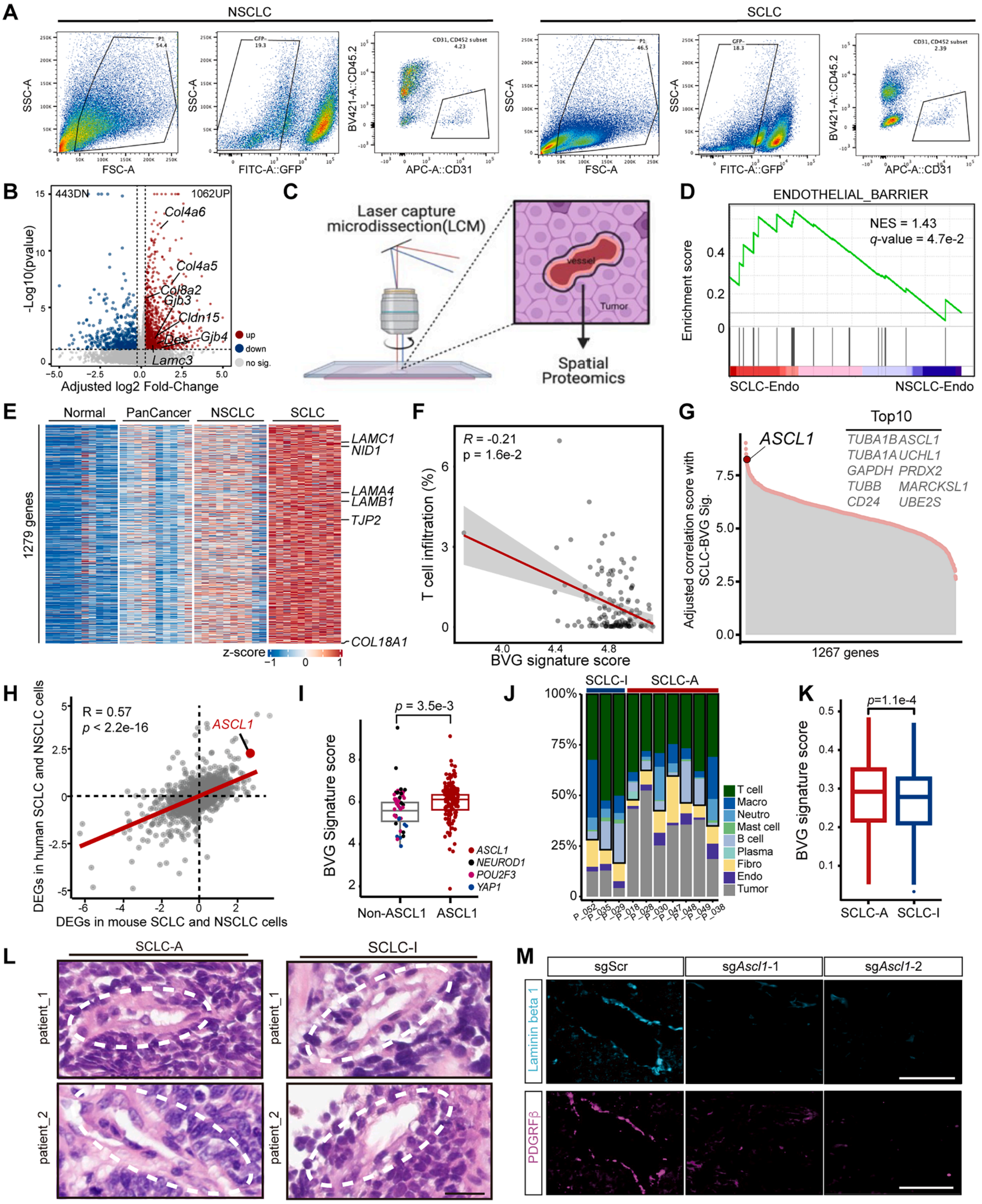

Figure S3. Additional features of the BVG in SCLC, related to Figure 3

(A) Representative flow cytometry plots illustrating the percentage of ECs (GFP$^-$CD31$^+$CD45$^-$) derived from NSCLC and SCLC tumors. GFP$^+$ tumor cells were excluded from the analysis (n = 3 mice per group).

(B) Volcano plot showing upregulated and downregulated genes in mouse-derived SCLC ECs compared to NSCLC. DEGs were defined as those with a $p < 0.05$ and an absolute adjusted log$_2$fold-change > 0.25. Basement membrane, junction-related genes are highlighted.

(C) Schematic representation of spatial proteomics outlining the segmented regions from mouse formalin-fixed paraffin-embedded (FFPE) samples. Briefly, the regions of tumor blood vascular regions were dissected using laser capture microdissection (with red blood cells within the luminal regions removed) for subsequent analysis.

(D) GSEA showed significant positive enrichment of the ENDOTHELIAL_BARRIER signature at the protein level in tumor blood vascular regions of mouse SCLCs compared to NSCLCs, as analyzed by spatial proteomics.

(legend continued on next page)

(E) Upregulated genes in SCLC-derived ECs (n = 524 cells) compared to those from normal lung tissues (n = 7,921 cells), pan-cancer tissues (n = 5,423 cells for BC; n = 7,605 cells for breast cancer; n = 1,515 cells for colorectal cancer; n = 207 cells for esophagus cancer; n = 2,655 cells for osteosarcoma; n = 3,268 cells for ovarian cancer; n = 1,227 cells for prostate cancer; n = 262 cells for hepatocellular carcinoma; n = 720 cells for lung squamous cell cancer; n = 1,353 cells for melanoma; n = 4,211 cells for renal cell carcinoma; n = 8,242 cells for GC), and lung adenocarcinoma tissues (n = 2,369 cells). Key genes are highlighted on the right.

(F) Correlation analyses between the T cell infiltration and BVG signature score in SCLC patients receiving immunotherapy, based on RNA-seq data from the Impower 133 cohort, n = 132.[33] p values were calculated using Spearman's rank correlation test.

(G) Scatter plot illustrating the adjusted correlation scores of 1,267 genes highly expressed in SCLC tumor cells from both SCLC mouse models and patient samples compared to NSCLC, correlated with the SCLC-BVG signature. The definition of the adjusted correlation score is provided in the STAR Methods section.

(H) Spearman's correlation coefficients between different expression genes DEGs from tumor cells in the SCLC and NSCLC mouse models (x axis) and patient data (y axis). Patient scRNA-seq data were acquired from Chan et al.[6]

(I) Boxplot comparing SCLC-BVG signature scores between non-ASCL1-type and ASCL1-type SCLC patients. RNA-seq data were reanalyzed from Liu et al.[9] and George et al.[45] (n = 194). Statistical significance was assessed using a two-sided Wilcoxon rank-sum test.

(J) Bar plots illustrating differences in cell-type proportions between SCLC-A (n = 7) and SCLC-I (n = 3) patients in the West China Hospital cohort.

(K) Boxplots showing BVG signature scores in ECs from SCLC-A and SCLC-I patients in the West China Hospital cohort. p values were calculated using a two-sided Wilcoxon rank-sum test.

(L) Representative H&E staining of paraffin-embedded SCLC-A and SCLC-I patient tumor samples in the West China Hospital cohort. Scale bars, 20 μm.

(M) Consecutive sections of SCLC tumors with sgScr and sg*Ascl1* were analyzed by IF for laminin beta 1 and PDGFRβ expression, as described in STAR Methods. Scale bars, 50 μm.

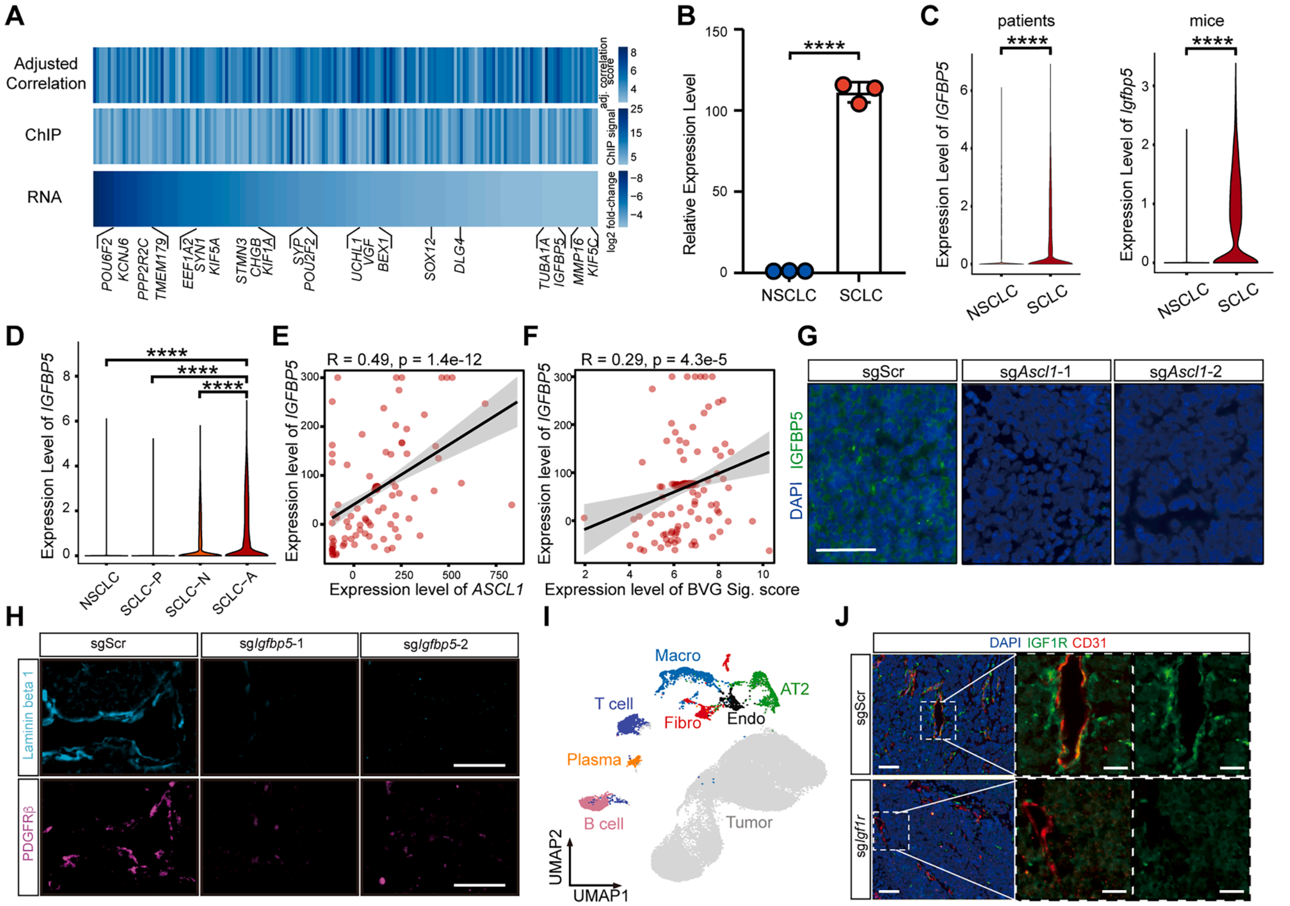

Figure S4. Additional characterization of the ASCL1-IGFBP5-IGF1R axis in BVG induction, related to Figure 4

(A) Heatmap showing adjusted correlation scores, chromatin immunoprecipitation (ChIP) signal values, and $\log_2$ fold-change of the 126 overlapping genes from Figure 4A, with $\log_2$ fold-change representing the RNA expression fold decrease after *Ascl1* knockout.

(B) The relative mRNA levels of *Igfbp5* in NSCLC and SCLC tumor cells. ****p* < 0.0001, *t* test, mean ± SD.

(C) Violin plots show the *IGFBP5* expression levels in patients (left) and mice (right) NSCLC and SCLC tumor cells (patient single-cell transcriptome data acquired from Chan et al., cohort), *****p* < 0.0001. Two-sided Wilcoxon rank-sum test.

(D) Violin plots illustrating the expression levels of *IGFBP5* in NSCLCs, SCLC-P (POU2F3$^+$) cancer cells, SCLC-N (NEUROD1$^+$) cancer cells, and SCLC-A (ASCL1$^+$) cancer cells from Chan et al.,[6] single-cell transcriptome cohorts, *****p* < 0.0001. Two-sided Wilcoxon rank-sum test.

(E and F) Correlation between the expression levels of *IGFBP5*, *ASCL1* (E), and SCLC-BVG signature (F) in SCLC patients (RNA-seq data acquired from Liu et al.[9] and George et al.,[45] *n* = 194). *p* values were calculated using Spearman's correlation test.

(G) IF analysis of IGFBP5 in consecutive sections of mouse SCLC tumors with sgScr or sg*Ascl1*, corresponding to the sections shown in Figure 3K. Scale bars, 50 μm.

(H) Consecutive sections of mouse SCLC tumors with sgScr and sg*Igfbp5* were analyzed by IF for the expression of laminin beta 1 and PDGFRβ, as described in STAR Methods. Scale bars, 50 μm.

(I) Uniform manifold approximation and projection (UMAP) plot of single-cell transcriptomes from sgScr and sg*Igfbp5* SCLC tumors.

(J) IF analysis of CD31 and IGF1R in mouse SCLC tumors with ECs infected with sgScr or sg*Igf1r*. Scale bars, 50 μm, magnified region, 20 μm.

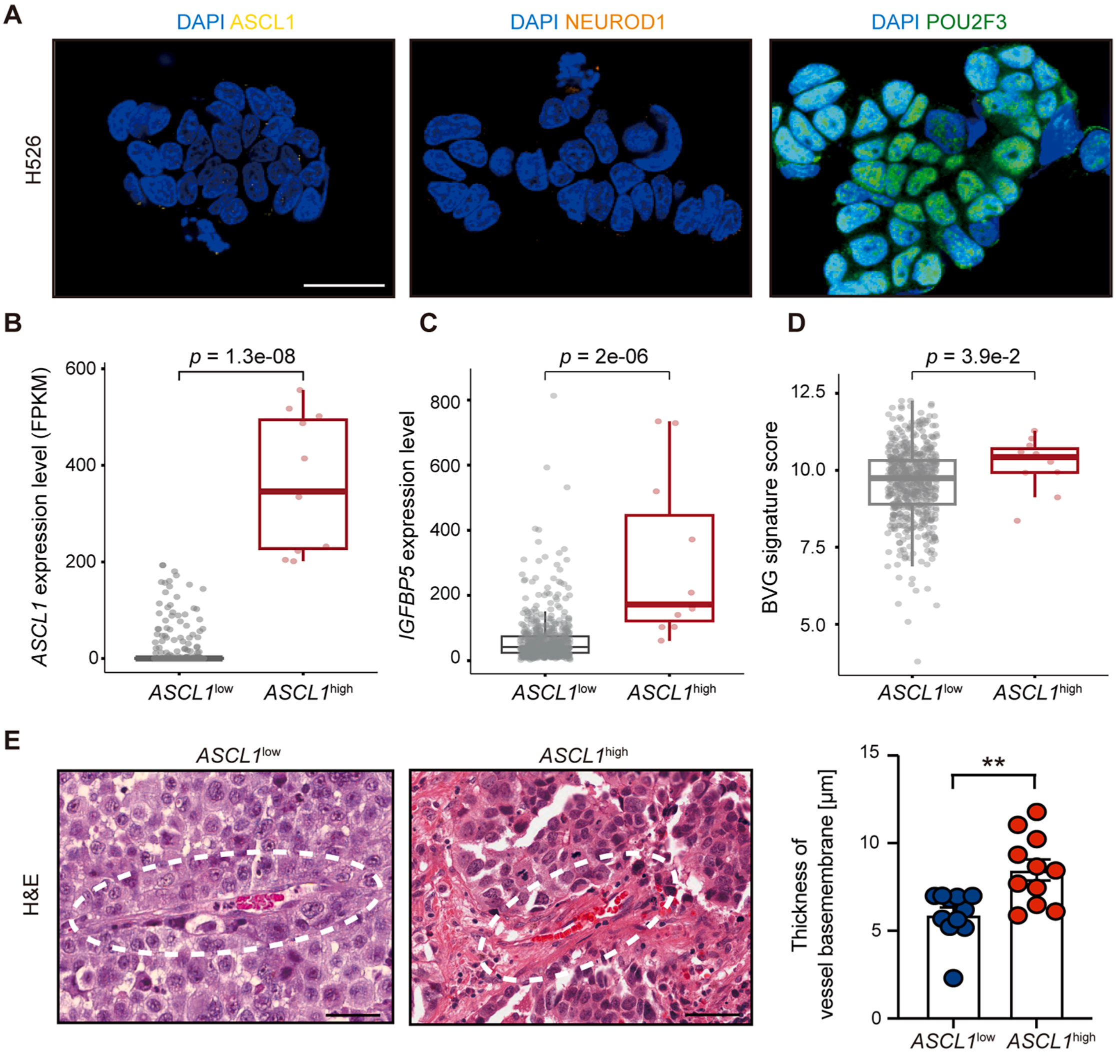

Figure S5. Additional evidence that ASCL1 and IGFBP5 are sufficient to induce the BVG structure, related to Figure 5

(A) Representative IF staining of ASCL1, NEUROD1, and POU2F3 of the SCLC human cell line H526 (SCLC-P). Scale bars, 25 μm.

(B–D) Boxplots showing *ASCL1*, *IGFBP5*, and BVG signature score expression levels in *ASCL1*^{high} (n = 11) and *ASCL1*^{low} (n = 583) NSCLC patients from the TCGA-LUAD cohort. p values were calculated using a two-sided Wilcoxon rank-sum test.

(E) Representative H&E staining of paraffin-embedded NSCLC tumors with low *ASCL1* or high *ASCL1* expression in patients from the TCGA. Scale bars, 50 μm. Bar plots quantify the average thickness of the BM in tumor blood vessels for tumor samples. $^{**}p < 0.01$. Mann-Whitney test, mean ± SEM of 11 biological replicate experiments.

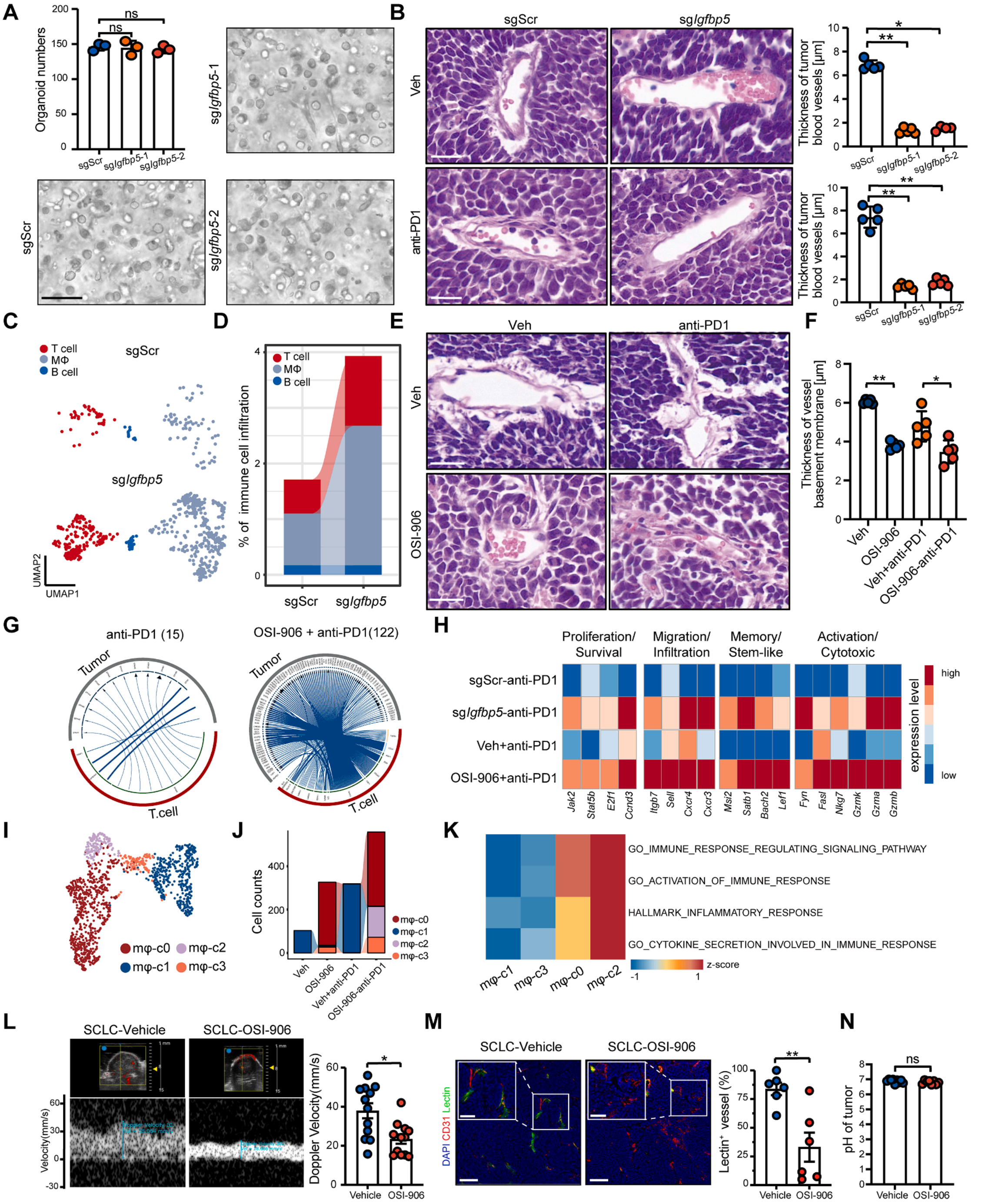

Figure S6. Additional analyses related to targeting the ASCL1-IGFBP5-IGF1R axis in SCLC, related to Figure 6

(A) Bar plots and bright-field images show the organoid numbers of SCLC tumors with sgScr or sg*Igfbp5*. Representative of 3 independent biological replicates. Ns, not significant, *t* test, mean ± SD. Scale bars, 100 μm.

(B) Representative H&E staining of paraffin-embedded mouse SCLC tumors with sgScr or sg*Igfbp5* treated with vehicle (up) or anti-PD1 (down). Scale bars, 20 μm. Bar plots quantify the average thickness of the BM in tumor blood vessels for tumor samples. $^{**}p < 0.01$. Mann-Whitney test, mean ± SD (n = 4–5 biological replicates).

(C) UMAP plot of immune cells transcriptomes from sgScr and sg*Igfbp5* SCLC mice treated with anti-PD1.

(D) Immune cell infiltration levels in sgScr and sg*Igfbp5* SCLC mice treated with anti-PD1.

(legend continued on next page)

(E and F) Representative H&E staining of paraffin-embedded mouse SCLC tumors treated with vehicle, anti-PD1, OSI-906, and anti-PD1 + OSI-906. Scale bars, 20 μm (E). Bar plots quantify the average thickness of the BM in tumor blood vessels for mouse tumor samples treated with vehicle, OSI-906, anti-PD1, and anti-PD1 plus OSI-906 (F). $^{*}p < 0.05$ and $^{**}p < 0.01$. Mann-Whitney test, mean ± SD of 5 biological replicates.

(G) Network of interactions between T cells and cancer cells in SCLC mouse tumors under anti-PD1 or OSI-906 plus anti-PD1 treatment conditions.

(H) Heatmap illustrating the expression patterns of cytotoxic, stem-like/memory, migratory/infiltrative, and proliferative/survival programs in $CD8^{+}$ T cells from sgScr- and sg*Igfbp5*- SCLC tumors treated with anti-PD1, as well as from SCLC tumors treated with anti-PD1 alone or anti-PD1 plus OSI-906 combination therapy.

(I) UMAP visualization of single-cell transcriptomes from macrophages in SCLC mice treated with vehicle, anti-PD1, OSI-906, or OSI-906 plus anti-PD1.

(J) Alluvial plots illustrating differences in macrophage subtype cell counts among mice treated with vehicle, anti-PD1, OSI-906, or OSI-906 plus anti-PD1.

(K) GSVA analysis showing activation scores of immune response-related pathways across macrophage subtypes.

(L) Representative Doppler ultrasound images showing measurement of tumor intratumoral blood-flow velocity. Bar plots quantify peak Doppler velocity (Vmax) in SCLC tumors treated with vehicle or OSI-906. $^{*}p < 0.05$, Mann-Whitney test. Data are shown as mean ± SEM (12 biological replicates).

(M) Representative fluorescent images of lectin perfusion of tumor vessels of SCLC tumors treated with vehicle or OSI-906. Scale bars, 100 μm. Magnified region, 50 μm. Bar plots quantify the $lectin^{+}$ vessels of SCLC tumors treated with vehicle or OSI-906. $^{**}p < 0.01$. Mann-Whitney test. Mean ± SEM of 6 biological replicates.

(N) Bar plots quantify tumor pH through SNARF-4F-based pH detection in SCLC tumors treated with vehicle or OSI-906. ns, not significant; Mann-Whitney test. Data are shown as mean ± SEM (n = 8–9 biological replicates).

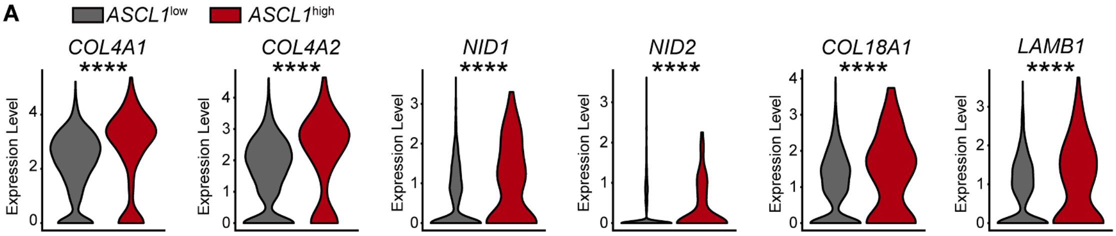

Figure S7. Basement membrane gene expression at single-cell resolution, related to Figure 7

(A) Violin plots illustrating the expression levels of BM-associated genes in ECs from castration-resistant prostate adenocarcinoma (n = 10) and NEC (n = 3) patients, based on scRNA-seq data from Chan et al.[3]